International Journal of Nanomedicine

Dovepress
Taylor & Francis Group

Open Access Full Text Article

ORIGINAL RESEARCH

Heparin-Conjugated Silver Nanoparticles via Amide Chemistry for Selective Targeting of Triple-Negative Breast Cancer and Pathogenic Fungi

Jayshree H Ahire[1], Qi Wang[2], Yongping Bao[2], Isabelle SR Storer[1,3], Stefan Bidula[1,3], Gary Rowley[3,4], Jason C Crack[1]

[1]School of Chemistry, Pharmacy and Pharmacology, University of East Anglia, Norwich, Norfolk, UK; [2]Norwich Medical School, University of East Anglia, Norwich, Norfolk, UK; [3]Centre for Microbial Interactions, Norwich Research Park, Norwich, Norfolk, UK; [4]School of Biological Science, University of East Anglia, Norwich, Norfolk, UK

Correspondence: Jayshree H Ahire, Email j.ahire@uea.ac.uk

Background: Heparin, a polydisperse glycosaminoglycan, is well-known for its anticoagulant activity and clinical use in preventing venous thromboembolism. In addition to coagulation, heparin and its derivatives have shown therapeutic potential in cancer and infectious, inflammatory, and neurodegenerative diseases. This study aimed to develop and evaluate heparin-capped AgNPs (hep-AgNPs) as multifunctional nanotherapeutics with selective cytotoxicity, antibacterial, and antifungal activity.

Methods: Heparin was covalently conjugated to cysteamine-terminated silver nanoparticles via MES-buffer-mediated amide coupling, providing a mild, aqueous alternative to conventional DMF-based methods. The nanoparticles were characterised by UV–Vis spectroscopy, Fourier-transform infrared spectroscopy (FTIR), nuclear magnetic resonance spectroscopy (NMR), dynamic light scattering (DLS), scanning electron microscopy (SEM) and energy-dispersive X-ray spectroscopy (EDX) analyses. The colloidal stability was assessed over a broad range of pH values. The biological performance of hep-AgNPs was evaluated in vitro against a triple-negative breast cancer (TNBC) cell line (MDA-MB-231), a double-positive cell line (MCF-7), and normal breast cells (MCF-10A), and microbial strains, including *Salmonella typhimurium, E. coli, Aspergillus fumigatus*, and *Candida albicans*.

Results: The synthesised hep-AgNPs exhibited high yield, effective heparin surface functionalization, and excellent colloidal stability at physiological pH, with stability systematically assessed across a broad pH range. Hep-AgNPs demonstrated time and concentration-dependent selective cytotoxicity, toward breast cancer cells, including MCF-7 and triple-negative MDA-MB-231, with a favourable selectivity index (>1) compared to MCF-10A cells, and the strongest selectivity observed in the TNBC model at 48 h. In addition, hep-AgNPs showed potent antibacterial activity (IC_{50} = 24.3 µg/mL) and antifungal activity (IC_{50} = 6.2 µg/mL for *A. fumigatus* and 24.43 µg/mL for *C. albicans*). In addition, they exhibit strong biocompatibility with keratinocytes and fibroblasts.

Conclusion: Heparin-capped silver nanoparticles combine the biological functionality of heparin with the antimicrobial and selective cytotoxic properties of the silver nanoparticles. Their selective cytotoxicity, antimicrobial efficacy, and favourable cellular interaction profiles highlight their potential as multifunctional nanoplatforms for applications such as chronic wound management in neutral to alkaline wound environments, and dose-controlled, targeted therapeutic strategies relevant to aggressive cancer models, including TNBC.

Keywords: heparin, silver nanoparticles, triple negative breast cancer, antibacterial, antifungal

Introduction

Nanotechnology has rapidly evolved into a dynamic and interdisciplinary field, offering transformative potential across biomedicine, materials science, and environmental applications.[1,2] At the nanoscale, materials exhibit distinctive physical and chemical behaviors, such as enhanced surface reactivity, quantum confinement effects, and tunable optical responses that arise from their small size and high surface-to-volume ratio.[3–7] Among the various nanomaterials, metal nanoparticles (MNPs) have garnered substantial interest owing to their catalytic activity, electrical and thermal conductivity, and unique optical properties.[8,9] Importantly, nanoparticles have been widely investigated as drug-delivery carriers due to their ability to improve

https://doi.org/10.2147/IJN.S576538
Received: 24 October 2025
Accepted: 30 January 2026
Published: 1 May 2026

Graphical Abstract

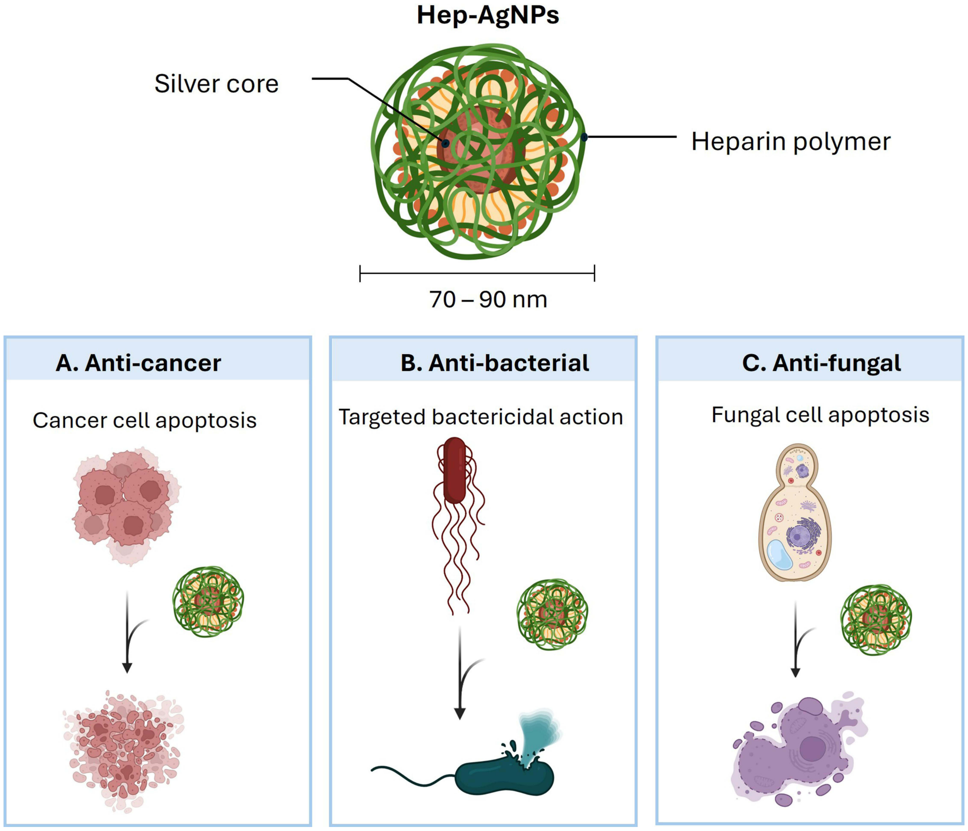

drug stability, enhance bioavailability, enable controlled or stimuli-responsive release, and facilitate targeted therapeutic delivery. Surface functionalization of MNPs further allows the conjugation of bioactive ligands, polymers, and biomolecules, enabling multifunctional platforms that integrate intrinsic physicochemical properties with therapeutic and diagnostic capabilities. These features have enabled their application in a wide range of technologies, including biosensing, targeted drug delivery, photothermal therapy, and bioimaging.[10]

While various metal nanoparticles, such as gold (AuNPs), copper (CuNPs), platinum (PtNPs), and zinc oxide (ZnO NPs), have demonstrated promising biological properties,[11–13] they each present specific limitations.[14] Gold nanoparticles, though highly biocompatible and easily functionalized, are cost-prohibitive for large-scale applications, and lacking inherent antimicrobial activity. Copper nanoparticles exhibit strong antibacterial effects, but are chemically unstable and prone to oxidation. Despite their excellent catalytic profiles, platinum and palladium NPs often exhibit low biocompatibility and synthetic complexity. ZnO nanoparticles, which are widely used in sunscreens and antibacterial coatings, can generate excessive reactive oxygen species, leading to unintended cytotoxicity. These limitations underscore the need for metal nanomaterials that combine stability, efficacy, biocompatibility, and multifunctionality.

Among noble metal nanostructures, silver nanoparticles (AgNPs) have emerged as one of the most widely studied and applied because of their broad-spectrum antimicrobial properties, strong surface plasmon resonance (SPR), and cytotoxicity against various cancer types.[15–17] AgNPs have been widely integrated into healthcare and consumer products, including antibacterial wound dressings[18,19] (eg Acticoat™), surgical bandages[20,21] (Silverlon®), catheters,[22,23] dental applications,[24,25] bone healing,[26,27] food packaging films,[28,29] textiles,[30,31] and personal care items[32] where antimicrobial coatings are essential. In biomedical research, AgNPs are also explored for antifungal therapies,[33] cancer-targeted drug delivery,[34,35] photothermal platforms,[36,37] and diagnostic applications.[38] The biological activity of AgNPs is commonly attributed to their ability to induce oxidative stress, disrupt microbial membranes, and interfere with intracellular pathways.[7,39]

Increasing evidence, however, supports a "Trojan Horse" mechanism, whereby AgNPs are internalised by cells and subsequently undergo intracellular oxidation, releasing Ag^+ ions within the cytosol. This process amplifies local oxidative stress and perturbs critical cellular functions, including mitochondrial activity and DNA integrity, making cellular uptake a key determinant of silver-mediated toxicity. Such uptake-driven mechanisms are particularly relevant in aggressive cancers, including triple-negative breast cancer (TNBC), where endocytic pathways are often upregulated.

However, many current formulations rely on unmodified or passively coated silver, which is prone to aggregation, lacks biological specificity, and may lead to cytotoxicity at higher concentrations.[40] These limitations highlight the ongoing need for functionalized AgNPs with improved stability, selectivity, and therapeutic precision, especially under physiological conditions.

To overcome these limitations, we propose a dual-functional strategy involving heparin, a sulfated glycosaminoglycan[41] with recognized biocompatibility and therapeutic versatility.[42,43] Heparin is well known for its clinical application as an anticoagulant and antithrombotic agent.[44] Beyond this established role, heparin exhibits a range of bioactive properties including anti-inflammatory effect,[45] antitumor activity,[46,47] angiomodulatory behaviour,[48] and regenerative potential,[49] making it a versatile therapeutic biomolecule. In particular, heparin has been reported to modulate angiogenesis—often exerting anti-angiogenic effects through interference with VEGF- and FGF-mediated signalling—which is highly relevant in cancer and wound-healing contexts. It has therefore been widely explored in wound healing, burn injury treatment, and inhibition of tumour metastasis.[50–55] Structurally, heparin enables selective interactions with numerous biological targets, including growth factors and cell surface receptors such as heparan sulfate proteoglycans (HSPGs), syndecans, and integrins, which are frequently dysregulated or overexpressed in cancer cells. These interactions provide a strong rationale for using heparin as a nanoparticle surface functionalising agent to promote selective cellular association and uptake. In cancer biology, heparin is also known to exhibit anti-adhesive and anti-migratory effects by modulating cell–matrix interactions and growth factor signalling, which may further influence tumour-associated cellular responses when presented on a nanoparticle surface. Recent evidence also supports the antibacterial activity of heparin, attributed to its potential to destabilise bacterial membranes, inhibit bacterial adhesion to host tissues, disrupt biofilm formation, and enhance immune cell responses.[21] Heparin has been further shown to increase pathogen susceptibility to host defences and antibiotics. Although its antimicrobial mechanisms have not yet been fully elucidated, the broad bioactivity and excellent biocompatibility of heparin make it an ideal candidate for nanoparticle surface functionalization aimed at enhancing biological performance across both cancer and microbial systems.

The combination of heparin and AgNPs offers a multifunctional nanotherapy platform. Heparin not only stabilises AgNPs but also modulates their selectivity and biological activity through targeted interactions with cellular receptors and components of the tumour microenvironment or microbial adhesion processes. This functionalization-mediated enhancement may enable effective activity at lower silver doses, thereby minimising off-target toxicity while amplifying therapeutic efficacy across multiple disease models. While heparin-functionalised nanomaterials and silver-based nanoparticles have each been explored separately for cancer targeting,[56] wound healing,[21,57] or antimicrobial applications,[58] the integrated evaluation of heparin-functionalised AgNPs across both cancer and infection-relevant models remains limited, particularly with respect to uptake behaviour, selectivity, and physicochemical constraints such as pH-dependent stability.

TNBC is an aggressive subtype lacking hormone or HER2 receptors, with limited targeted treatment options and a high risk of recurrence. In parallel, the global rise of antimicrobial resistance and the prevalence of chronic, infection-prone wounds highlight the need for multifunctional therapeutic platforms capable of addressing both malignant and infectious pathologies. Moreover, chronic wounds often present complex microenvironments involving persistent infection, impaired healing, and inflammation, underscoring the clinical need for materials that combine antimicrobial activity with controlled biological interactions.

In this paper, we report the synthesis and surface functionalization of heparin-capped AgNPs (hep-AgNPs) via a covalent amide coupling strategy using cysteamine-functionalized AgNPs. The resulting nanoconjugates were thoroughly characterised by UV-Vis spectroscopy, nuclear magnetic resonance spectroscopy (NMR), Fourier-transform infrared spectroscopy (FTIR), dynamic light scattering (DLS), scanning electron microscopy (SEM), and energy-dispersive X-ray spectroscopy

(EDX), X-ray diffraction (XRD), thermogravimetric analysis (TGA) and zeta potential analysis to assess their structure, stability, and surface chemistry. We evaluated their colloidal behaviour across a wide pH range (2–9) and assessed their biological performance, including selective cytotoxicity against TNBC cell lines (MCF-7 and MDA-MB-231); antimicrobial activity against *Escherichia coli, Salmonella typhimurium, Candida albicans*, and *Aspergillus fumigatus*; and cellular uptake via ICP-MS. Furthermore, their compatibility with keratinocytes and fibroblasts was evaluated to support their applications in wound healing. Collectively, our findings highlight hep-AgNPs as a multifunctional nanoplatform demonstrating concentration-dependent selective cytotoxicity, together with antibacterial and antifungal activities.

Materials and Methods

Material

Silver nitrate ($AgNO_3$) and dimethylaminopyridine (DMAP) were purchased from Fisher Scientific (UK). Sodium borohydride ($NaBH_4$), 2-mercaptoethylamine hydrochloride (cysteamine), *N*-(3-dimethylaminopropyl)- *N*-ethylcarbodiimide hydrochloride (EDC), *N*-hydroxysuccinimide (NHS), tetrahydrofuran (THF), *N,N*-dimethylformamide (DMF), Heparin Sodium salt from the porcine mucosa, dimethyl sulfoxide (DMSO), and 3-(4,5-dimethyl-2-thiazolyl)-2,5-diphenyl tetrazolium bromide (MTT) were purchased from Sigma-Aldrich.

Synthesis of Amine Capped Silver Nanoparticles (Cyst-AgNPs)

Amine-terminated AgNPs were synthesised by the reduction of silver nitrate using cysteamine hydrochloride as a stabilising agent. This method follows the protocols from our recently published work.[21] In a typical reaction setup, 20 mL of DMF was placed in an Erlenmeyer flask equipped with a magnetic stirrer. The flask was submerged in an ice bath. Subsequently, an aqueous solution of cysteamine (0.7 mmol, 0.5 mL) and $AgNO_3$ (0.234 mmol, 0.5 mL) was added to the flask. The mixture was stirred for 10 min, following which $NaBH_4$ (3 mL, 210 mM in water) was added dropwise. This addition resulted in a rapid colour change from milky white to yellowish-brown. The reaction mixture was then stirred for an additional 30 min. Following the reaction, the cyst-AgNPs were collected and purified via centrifugation at 8000 rpm for 10 min and then washed three times with DMF. The final dark brown pellet of synthesised nanoparticles was resuspended in water.

Synthesis of Heparin Capped Silver Nanoparticles (Hep-AgNPs)

Heparin-capped silver nanoparticles (hep-AgNPs) were synthesized using an amide coupling reaction, adapted from our previous work.[21] It should be noted that, unlike molecular reagents, nanoparticles do not possess a fixed molecular weight; therefore, stoichiometric ratios were defined relative to the molar concentration of nanoparticles rather than silver atoms.

The concentration of cyst-AgNPs was estimated from UV–Vis absorbance at ~400 nm using the Beer–Lambert law and a reported extinction coefficient for spherical AgNPs with a core diameter of ~10–11 nm. Based on the calculated nanoparticle number concentration (Nparticles mL^{-1}), “1 equivalent” of cyst-AgNPs refers to this molar nanoparticle concentration.

The number of surface-accessible amine groups per nanoparticle was estimated from the nanoparticle surface area, assuming spherical geometry, following the approach described by Oliva et al, which predicts approximately ~30 reactive sites per AgNP of this size. On this basis, heparin-to-nanoparticle ratios (1:1, 1:2, 1:4, and 1:12) were defined relative to the estimated number of surface amine groups rather than bulk silver content.

For a representative synthesis, In a 25 mL round-bottom flask, a mixture of heparin sodium salt (2 eq relative to nanoparticle concentration, 48 mg), EDC (8 eq), NHS (8 eq), and a catalytic amount of DMAP was combined and stirred at room temperature in the presence of MES buffer (0.5M, 5 mL) and stirred at room temperature for 2 h to activate the carboxyl groups of heparin. Subsequently, cyst-AgNPs (1 eq, corresponding to the calculated nanoparticle molar concentration; 24 mg total AgNP mass) were added, and the reaction mixture was stirred overnight. The resulting hep-AgNPs were precipitated using ethanol and acetone to remove excess coupling reagents and purified using centrifugal filtration (30 kDa MWCO) at 10,000 rpm for 5 min, followed by three washes with water. While centrifugal filtration effectively removes unreacted heparin and excess coupling reagents, we note that trace amounts of low–molecular weight buffer components (eg MES) may persist despite multiple wash cycles. Performing dialysis (MWCO 12–14 kDa) against water removes residual MES buffer and reaction byproducts. The purified hep-AgNPs were finally redispersed in water prior to characterization.

Characterization of Silver Nanoparticles

The hep-AgNPs were extensively characterized to confirm their structural and functional properties. Various analytical techniques have been used for this purpose, including UV–Vis absorption spectroscopy, nuclear magnetic resonance (NMR) spectroscopy, Fourier transform infrared (FTIR) spectroscopy, scanning electron microscopy (SEM), energy-dispersive X-ray spectroscopy (EDX), thermogravimetric analysis (TGA), X-ray diffraction (XRD), zeta potential analysis, and dynamic light scattering (DLS).

UV–Vis absorption measurements were performed using a PerkinElmer 35 double-beam spectrometer with a disposable cuvette. FTIR analysis was performed on the solid samples of hep-AgNPs using a PerkinElmer ATR-FTIR spectrometer. DLS analysis was conducted using a Zetasizer Nano ZS (Malvern Instruments Ltd., UK) to determine the hydrodynamic diameter, polydispersity, and surface charge of the nanoparticles.

Scanning electron microscopy (SEM) and energy-dispersive X-ray spectroscopy (EDX) were performed using a Zeiss Gemini 300 system equipped with a Quorum Technologies cryosystem and an Oxford Instruments EDS. For these analyses, a diluted suspension of hep-AgNPs in ethanol was drop-cast onto a 200-mesh carbon-coated copper grid, which was then dried prior to imaging.

XRD measurements were performed using a Rigaku SmartLab SE powder diffractometer with 10 mg of powdered hep-AgNPs.

Cell Culture

The cytotoxicity of the synthesised hep-AgNPs was evaluated in the MCF-7, MDA-MB-231, MCF-10A, HaCaT, and L929 cell lines. The normal breast epithelial cell line MCF-10A was obtained from American Type Culture Collection (ATCC) (LGC Standards, London, UK). The MCF-10A normal breast cell line was cultured in DMEM (Dulbecco's modified Eagle's medium) /F12 (Gibco, Thermo Fisher Scientific, Paisley, UK) enriched with 5% horse serum (Gibco, Thermo Fisher Scientific, Paisley, UK), hydrocortisone at 0.5 mg/mL, epidermal growth factor (EGF) at 20 ng/mL (Peprotech, London, UK) and insulin at 10 µg/mL (Sigma Aldrich, Gillingham, Kent, UK), maintained at 37°C with 5% CO_2. MCF-7, MDA-MB-231, HaCaT, and L929 cells were maintained in DMEM supplemented with 10% foetal bovine serum (FBS), 2 mM glutamine, penicillin (50 U/mL), and streptomycin (50 ug/mL) (Gibco, Thermo Fisher Scientific, Paisley, UK) in a humidified environment at 37°C with 5% CO_2.

Evaluation of Cytotoxicity

The cytotoxicity of the hep-AgNPs was evaluated using the MTT assay, which assesses mitochondrial dehydrogenase activity as an indicator of cell viability. Cells were seeded in 96-well plates at a density of 5000 cells per well and incubated for 24 h prior to treatment. In this method, a sterile filtered MTT stock solution in phosphate-buffered saline (PBS) pH 7.4 (5 mg/mL) was added to each well of a 96-well plate, resulting in a final concentration of 0.5 mg/mL. After 2 h of incubation, the unreacted dye was removed and the insoluble formazan crystals were dissolved in 100 µL of DMSO. The absorbance was measured at 570 nm with a reference wavelength of 690 nm using a microplate reader (BMG Labtech Ltd., Aylesbury, UK). The cell viability (%) was calculated using the following formula: cell viability (%) = ODtest/ODcontrol × 100%.

Bacterial Culture and Treatment Condition

Gram-negative *Salmonella enterica serovar* Typhimurium SL1344 was maintained on Lysogeny Broth (LB) agar plates. For the experiments, 10 mL of the overnight culture was grown in LB broth at 37°C with shaking at 180 rpm. The overnight culture was then diluted 1:100 in fresh LB medium and silver nanoparticles (Hep-AgNPs) were added at the specified concentrations. Cultures were incubated at 37°C with aeration for 24 hours, after which bacterial growth was assessed by measuring the optical density at 600 nm (OD_{600}).

Antifungal Activity

Susceptibility testing was performed according to EUCAST guidelines with the following modifications: after 24 h, resazurin (AlamarBlue) was added to each well of the microdilution plate to quantify the conversion to resorufin as an indicator of cell viability. Testing for *C. albicans* was performed according to EUCAST Definitive Document 7.4, and testing for *A. fumigatus* was performed according to EUCAST Definitive Document 9.4. Susceptibility assays were performed in triplicate. Microdilution plates were read at 560 nm excitation / 590 nm emission filter set and viability was calculated as a percentage of the untreated control. The readings were taken after 24 h (the usual endpoint for *C. albicans*) and 48 h (the usual endpoint for *A. fumigatus*). Images were acquired using an EVOS XL Core Imaging System and were acquired at high magnification (40× objective) under identical imaging conditions. The minimum inhibitory concentrations for 90% (MIC90) and 50% (MIC50) metabolic activity inhibition were calculated using GraphPad Prism version 10.

Assessment of Uptake of Hep-AgNPs by ICP-MS Analysis

The Ag content was determined using inductively coupled plasma mass spectrometry (A Thermo iCAP™ TQ-ICP-MS technique). The silver content was calculated and is presented as a function of time. Each experiment was performed in triplicates.

ICP-MS Analysis for MDA-MB-231 Cells

MDA-MB-231 cells were seeded in 6-well plates and exposed to the IC_{50} concentration of hep-AgNPs (20 µg/mL) for 0, 3, 6, and 24 hours. At each time point, the cells were washed thrice with phosphate-buffered saline (PBS) to remove any non-internalised or loosely bound nanoparticles. The washed cells were initially resuspended in 2% nitric acid to promote nanoparticle dissolution and then stored at − 80 °C prior to digestion. For ICP-MS analysis, 1 mL of the sample was digested with 3 mL of ultra-pure HNO_3, ensuring the complete dissolution of silver. After digestion, the sample was diluted with Milli-Q water to reduce matrix effects. The silver content was quantified by detecting ^{109}Ag using ICP-MS, and uptake was expressed as nanograms of silver per cell and normalised to the cell count.

ICP-MS Analysis Method for Fungal Cells

Intracellular accumulation of hep-AgNPs was evaluated in *C. albicans* and *A. fumigatus* after 3, 6, 24, and 48 h. Experiments were conducted in triplicate at each time point, including the untreated controls. The fungal cells were exposed to hep-AgNPs at their respective IC_{50} concentrations: 24.4 µg/mL for *C. albicans* and 6.2 µg/mL for *A. fumigatus*.

Briefly, *A. fumigatus* and *C. albicans* were cultured on Sabouraud dextrose agar for 48 and 24 h, respectively. *A. fumigatus* conidia were harvested and normalised to 1×10^5 CFU/mL, and *C. albicans* cells were normalised to 1.5×10^5 CFU/mL in RPMI-1640. The cultures were treated with hep-AgNPs and incubated under standard growth conditions. At each time point, the cells were harvested and centrifuged at 5000 rpm for 5 min prior to washing thrice with sterile PBS to remove unbound nanoparticles. The resulting cell pellets were stored at − 80 °C until further processing. For ICP-MS analysis, 1 mL of the fungal cell sample was digested with 3 mL of ultra-pure HNO_3, ensuring complete dissolution of silver. After digestion, the sample was diluted with Milli-Q water to reduce matrix effects. Silver uptake was quantified by measuring the ^{109}Ag isotope using ICP-MS, and values were normalised to the cell number to calculate the uptake in ng/cell.

ICP-MS Analysis Method for Bacterial Cells

To quantify the intracellular accumulation of hep-AgNPs in *S. typhimurium*, bacterial cultures were treated with hep-AgNPs at an IC_{50} concentration of 20 µg/mL at four time points: 0, 2, 8, and 24 h. All experiments were conducted in triplicate, including untreated controls.

Briefly, *S. typhimurium* was cultured in nutrient broth and incubated at 37 °C with shaking until the logarithmic growth phase was reached. The bacterial suspension was then treated with hep-AgNPs and incubated under the same conditions. At each time point, 1 mL of the culture was harvested by centrifugation at 10,000 rpm for 5 min. The cell pellets were washed three times with sterile PBS to eliminate unbound nanoparticles. The washed pellets were stored at − 80 °C until digestion. Prior to ICP-MS analysis, 1 mL of the sample was digested with 3 mL of ultra-pure HNO_3, ensuring the complete dissolution of silver. After digestion, the sample was diluted with Milli-Q water to reduce matrix effects. The silver content was quantified by detecting ^{109}Ag using ICP-MS, and uptake was expressed as nanograms of silver per bacterial cell and normalised to the cell count.

Statistical Analysis

Statistical analyses were performed using GraphPad Prism version 8.0.2 (GraphPad Software, San Diego, CA, USA). All quantitative data are presented as mean ± standard deviation (SD) from at least three independent experiments. For cell viability and multi-species uptake assays, a Two-way Analysis of Variance (ANOVA) was employed, followed by Dunnett's post-hoc tests for multiple comparisons as appropriate. The half-maximal inhibitory concentration (IC50) was determined using non-linear regression analysis (log(inhibitor) vs normalized response). For the antimicrobial activity and single-variable uptake assays, differences between groups were analyzed using a One-way ANOVA followed by Dunnett's multiple comparisons test to compare treatment groups against the control. A P-value of $p< 0.05$ was considered statistically significant. Significance levels are indicated in the figures as $^{*}p < 0.05$, $^{**}p < 0.01$, $^{***}p < 0.001$.

Results

Physiochemical Characterization

Synthesis and Characterization of Heparin Capped Silver Nanoparticles (Hep-AgNPs)

The synthesis of hep-AgNPs was performed according to our recently published method.[21] Scheme 1 illustrates the synthesis of hep-AgNPs from cyst-AgNPs via an amidation reaction using EDC and NHS as coupling reagents. Well-characterised and purified cyst-AgNPs were incubated with heparin overnight in MES buffer (0.5 M, pH 5.2).

In our previous study, the reaction was performed in anhydrous DMF under an inert atmosphere to minimise the hydrolysis of the EDC-activated intermediate. However, this approach was only partially successful because of the poor solubility of heparin in DMF. Although DMF is a polar aprotic solvent, it lacks the hydrogen bonding and ionic stabilisation required to dissolve highly charged polyanions, such as heparin. The direct dissolution in DMF resulted

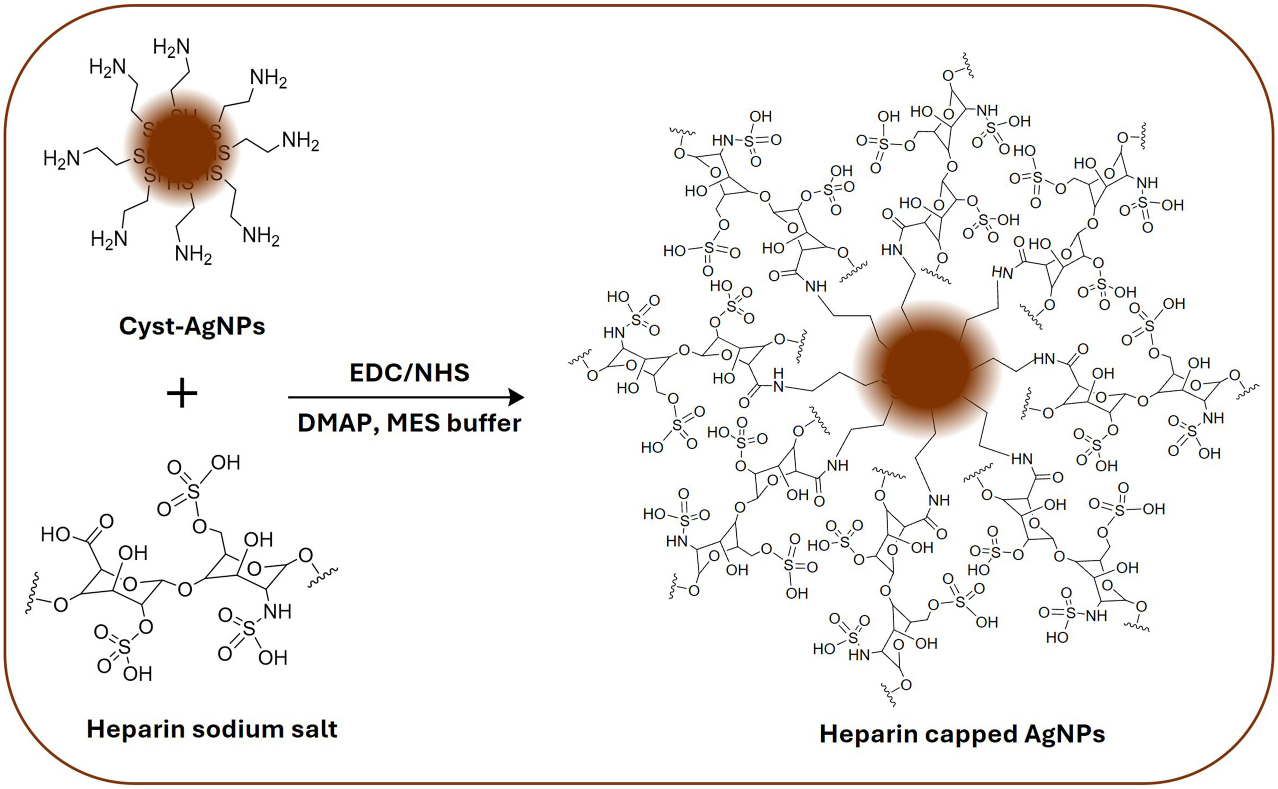

Scheme 1 Schematic representation of synthesis of heparin capped silver nanoparticles from cyst-AgNPs and heparin through amidation reaction.

in clumping and precipitation. Although the obtained product was relatively pure and showed evidence of heparin capping on the AgNP surface, the precipitation of heparin suggests inefficient surface functionalization. Moreover, the reaction requires longer time to proceed under inert atmospheric conditions.

To overcome these limitations and improve both capping efficiency and reaction kinetics, in the present work we employed MES buffer as the reaction medium. The polyanionic nature of heparin, arising from its highly sulfated and carboxylated structure, dictates its solubility. The strong negative charges on the sulfate and carboxylate groups generate extensive hydration shells, rendering heparin highly hydrophilic and poorly soluble in organic solvents where such interactions cannot be maintained. The instability of cyst-AgNPs under these conditions poses another challenge. This instability is attributed to the ionisation state of the surface coating, which is influenced by the net charge of the amine layer and is highly sensitive to the pH of the dispersing medium. Considering these factors, MES buffer (pH 5.2) was chosen as the reaction solvent. MES buffer offers several advantages: it maintains the stability of cyst-AgNPs by providing an appropriate pH environment, improving the solubility of heparin, and creating favourable conditions for the amidation reaction. Although hydrolysis of the EDC-activated intermediate is a concern in aqueous media, the inclusion of NHS and DMAP stabilises the intermediate and facilitates the coupling reaction. DMAP, a nucleophilic catalyst, enhances the amidation reaction by accelerating the process and improving efficiency, particularly in aqueous environments. Thus, the MES buffer not only avoided interference but also enhanced the efficiency of the reaction, enabling the successful synthesis of hep-AgNPs.

The surface functionalization of hep-AgNPs was further optimised by exploring various ratios of heparin to cyst-AgNPs. Each reaction with cyst-AgNPs typically yielded 20–24 mg of nanoparticles. Based on calculations by Oliva et al,[59] each cyst-AgNP had approximately 30 active sites available for further reactions However, this number depends on several factors, including the nanoparticle size, shape, reaction time, and temperature. Using this assumption, various ratios of AgNPs to heparin were tested, specifically 1:4, 1:2, and 1:1, to systematically investigate optimal surface functionalization. These ratios were analysed using UV-vis spectroscopy and FTIR to evaluate the degree of functionalization. Additionally, the efficacy of these ratios was evaluated in both the cellular and bacterial models to assess the performance of the material, as shown in Supplementary Figures 1 and 2. The cytotoxicity profiles of hep-AgNPs with varying Ag: heparin ratios were examined in HaCaT and L929 cell lines as well as in *E. coli* for 24 and 48 h. These results are verified and discussed in the Discussion section.

Heparin is a sulfated glycosaminoglycan mixture that consists of unbranched polysaccharide chains composed of 15 to 100 alternating monosaccharide units of L-iduronic acid and D-glucosamine and has an active carboxylic acid group at every segment. Therefore, during the amidation reaction, each acidic group was expected to react with the NH_2 groups of the Ag nanoparticles which wrapped the surface of the nanoparticles, as shown in Figure 1. Consequently, it is likely that the polymer was wrapped around the nanoparticles as it reacted. Through this process, some of the NH_2 groups are expected to be unreacted.

The synthesised hep-AgNPs were characterised using UV-vis spectroscopy (Supplementary Figure 3a), which exhibited a strong absorption peak at approximately 450 nm, indicative of the surface plasmon resonance (SPR) phenomenon of (Ag). The size and hydrodynamic diameter of the hep-AgNPs were further confirmed using SEM (Figure 2a) and DLS spectroscopy (Supplementary Figure 3b). SEM images revealed monodisperse nanoparticles with a size range of 11 ± 3 nm. DLS analysis (Supplementary Figure 3b) of hep-AgNPs showed an increase in the overall hydrodynamic diameter to 70–90 nm, further supporting the successful conjugation of cyst-AgNPs with heparin. In comparison with cyst-AgNPs, as reported in our recent article,[21] SEM analysis (Figure 2a (inset)) showed slight aggregation or clustering of cyst-AgNPs. However, after functionalization with heparin, the inter-particle distance increased, indicating successful functionalization. This effect can be attributed to the long-chain polymer structure and high molecular weight (15 kDa) of heparin, which effectively wraps around the nanoparticles, stabilising them and reducing aggregation.

EDS analysis was performed to confirm the elemental composition of hep-AgNPs (Figure 2b). The spectrum shows strong characteristic peaks for Ag, confirming the successful formation of AgNPs. In addition to silver, signals corresponding to carbon (C), oxygen (O), and sulfur (S) originate from the heparin coating. The presence of sulfur is particularly significant, as it reflects the sulfate groups of heparin and further supports the successful surface functionalization of AgNPs. Notably, the

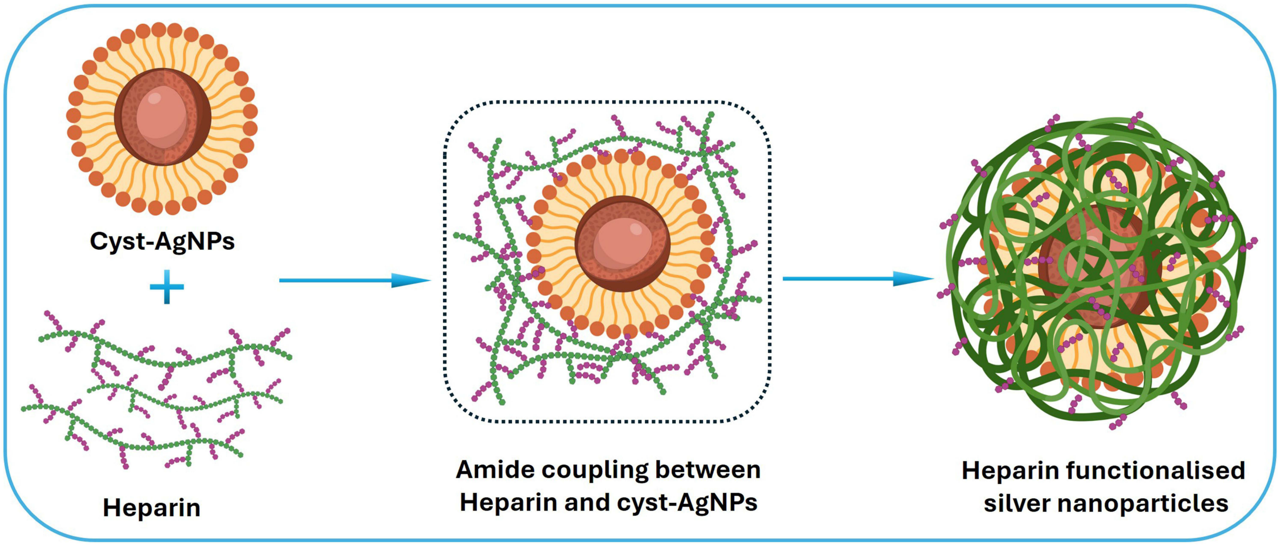

Figure 1 A graphical representation of amide coupling reaction between cyst-AgNPs and heparin.

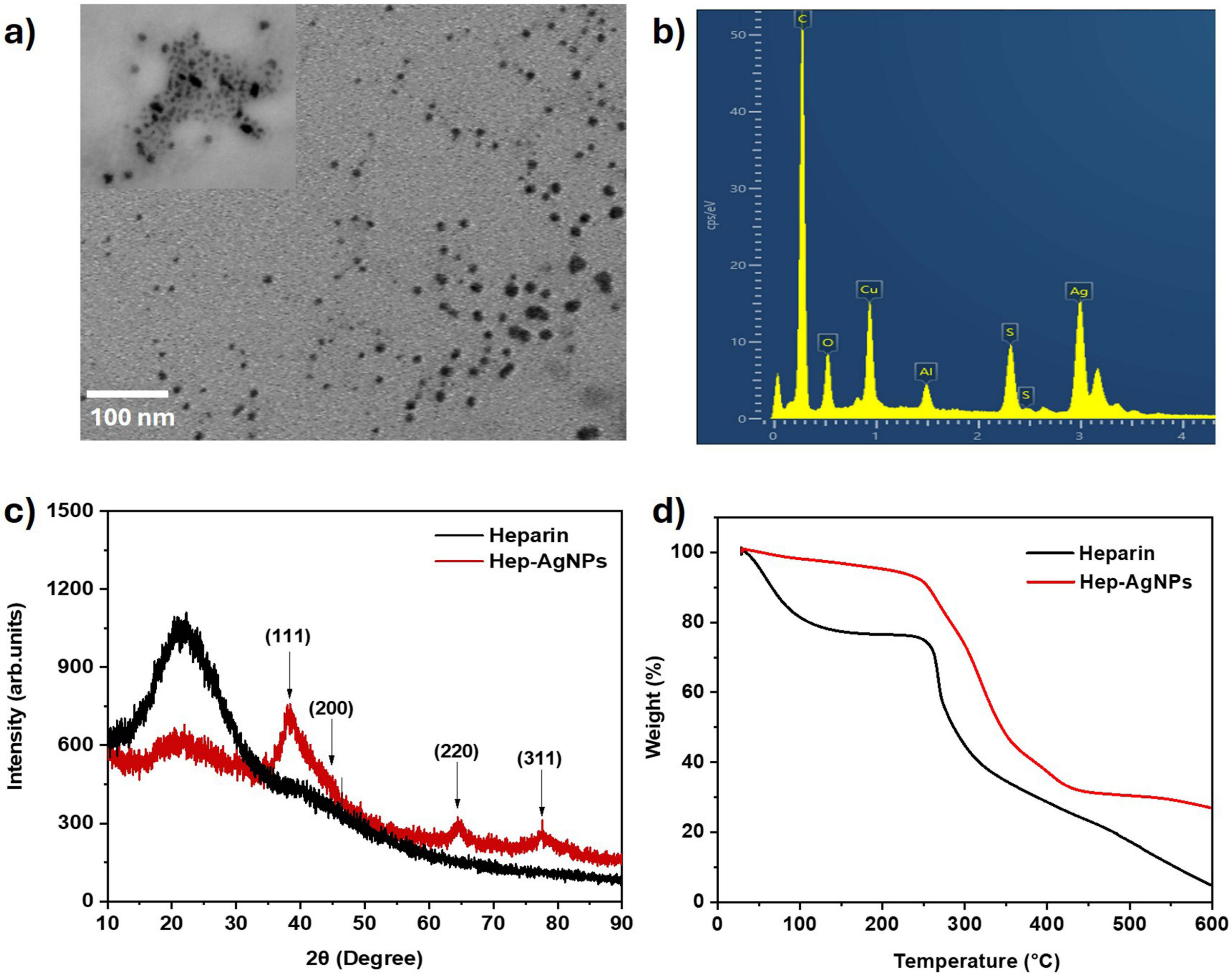

Figure 2 (**a**) SEM images of hep-AgNPs, including an inset showing cyst-AgNPs, (**b**) EDS spectra confirming the elemental analysis of hep-AgNPs. (**c**) X-ray diffraction patterns of hep-AgNPs (red) compared with heparin (black), highlighting the crystalline nature of the silver nanoparticles. (**d**) displays the thermogravimetric analysis of hep-AgNPs (red) and heparin (black), demonstrating the thermal stability of the silver core and the distinct degradation profiles of the organic components.

sulfur signal was more pronounced than that of our previously reported material, in which only a small sulfur peak was observed. This increase can be attributed to the use of the MES buffer as the reaction medium, as MES contains a sulfonic acid group that also contributes to the sulfur signal.

The crystalline structure of hep-AgNPs was evaluated by XRD analysis, as shown in Figure 2c. The XRD pattern of hep-AgNPs (red) was compared with that of the pure heparin polymer (black). The hep-AgNPs exhibited four distinct and narrow diffraction peaks at 38.10°, 44.13°, 64.34°, and 77.37°, which corresponded to the (111), (200), (220), and (311) planes of face-centred cubic (fcc) metallic silver, respectively (JCPDF Card No: 04-0783). In contrast, the XRD pattern of heparin alone displayed a broad peak centred at approximately 24°, indicating its amorphous, non-crystalline structure. The XRD profile of hep-AgNPs also showed a broad hump at 24°, confirming the presence of a heparin coating on the nanoparticle surface. The sharp and intense peaks of Ag in the hep-AgNP spectrum confirmed the formation of highly crystalline AgNPs. Importantly, no peaks corresponding to silver oxide (Ag_2O) were observed which usually appears at 32.9° or 55.0°, suggesting that heparin capping effectively protects the silver core from oxidation.

Thermogravimetric analysis was conducted to evaluate the thermal stability and composition of the heparin and hep-AgNPs, as shown in Figure 2d. The TGA curve of pure heparin showed a typical two-step degradation profile. The initial weight loss below 150°C was attributed to the loss of moisture and bound water, followed by major decomposition between 250°C and 400°C, corresponding to the breakdown of the sulfated polysaccharide backbone. The residual weight at 600 °C was approximately 10–15%, likely due to non-volatile inorganic salts and thermally stable sulfate residues.

In contrast, hep-AgNPs exhibited a slightly delayed but more significant weight loss, with a sharper degradation slope in the 250–400 °C range and a higher residual mass (~20–30%) at 600 °C. This enhanced weight loss suggests a higher heparin content associated with the nanoparticle surface and potential catalytic effects of silver, which promotes more efficient thermal decomposition of the organic coating. The absence of a distinct third degradation step indicates a residual metallic core content or fine dispersion of AgNPs within the matrix. These findings further suggest that heparin wraps around the nanoparticle surface and forms a thick layer around it, resulting in a relatively low density of silver compared to the heparin polymer. These results confirm the successful capping of AgNPs with heparin and illustrate the impact of surface functionalization on the thermal behaviour of the nanoparticles.

Chemical Characterization (FTIR and NMR Analysis)

The hep-AgNPs were further characterised using FTIR and ^1H NMR spectroscopy to confirm the surface functionalization and formation of amide bonds between the amine-functionalized AgNPs and heparin. As shown in Figure 3, the ^1H NMR spectra of the hep-AgNPs (red) were compared with those of heparin (green) and NH_2-AgNPs (brown). The signals observed in the range of 3.0–3.7 ppm and 5.0–5.4 ppm in the hep-AgNP spectrum correspond to the protons of glucosamine and iduronic acid residues, characteristic of heparin. Notably, a new peak at δ 2.9 ppm was detected, which can be attributed to methylene protons introduced through covalent linkages with NH_2-AgNPs. However, a significant overlap with MES buffer signals was observed in the 2.3–3.3 ppm region, arising from the morpholine ring and ethanesulfonic acid side chain. This overlapped with the expected amide bond resonances and peaks from cyst-AgNPs, indicating that the sample still contained residual MES buffer and required further purification. Despite this interference, the presence of additional signals between δ 1.5–3.0 ppm supports the formation of amide linkages, confirming the successful covalent conjugation of heparin to the AgNP surface.

To further investigate the conjugation of heparin to cyst-AgNPs, surface modification of hep-AgNPs was verified using FTIR spectroscopy (Figure 4). A notable absorption band around 1695 cm^{-1} indicates the formation of amide bonds, signifying a covalent interaction between the carboxyl groups of heparin (typically observed near 1648 cm^{-1}) and the amine functionalities of cysteamine-coated AgNPs. A peak appearing at 1558 cm^{-1} is attributed to N–H bending, further supporting the presence of the amide linkage. Additional peaks observed between 1200 and 1400 cm^{-1} reflect the symmetric and asymmetric vibrations of sulfonate ($–SO_3$) and sulfate ($–SO_4$) groups, characteristic of heparin's sulfated structure. The region spanning 989–1187 cm^{-1} corresponds to the C–O–C bond stretching originating from the polysaccharide backbone. Broad absorptions between 3000 and 3700 cm^{-1} are due to hydroxyl (–OH) stretching and possibly residual amine ($–NH_2$) groups. Peaks in the 2800–2900 cm^{-1} range relate to aliphatic C–H vibrations, present in both the

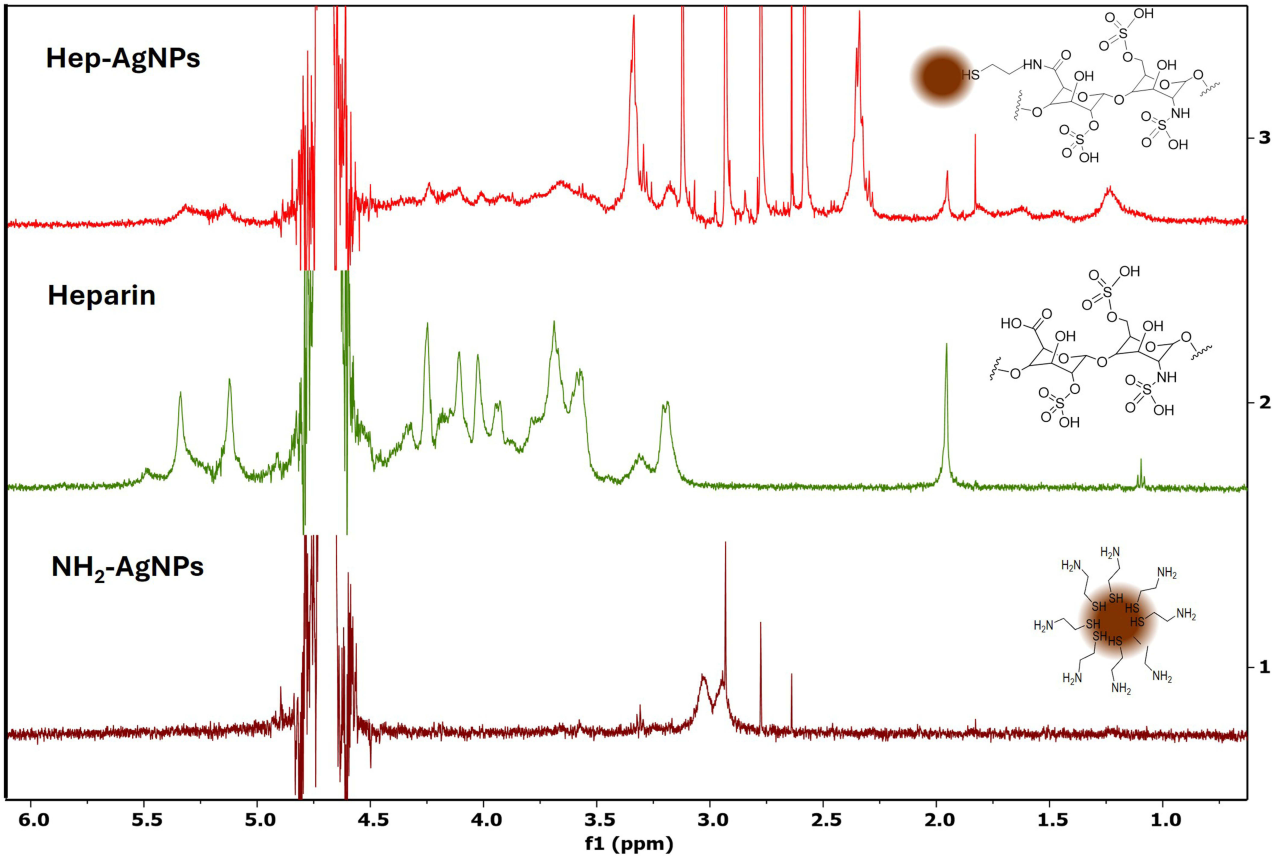

Figure 3 ^{1}H NMR spectra of heparin-capped silver nanoparticles in D_2O comparing with cysteamine-functionalized silver nanoparticles and pure heparin.

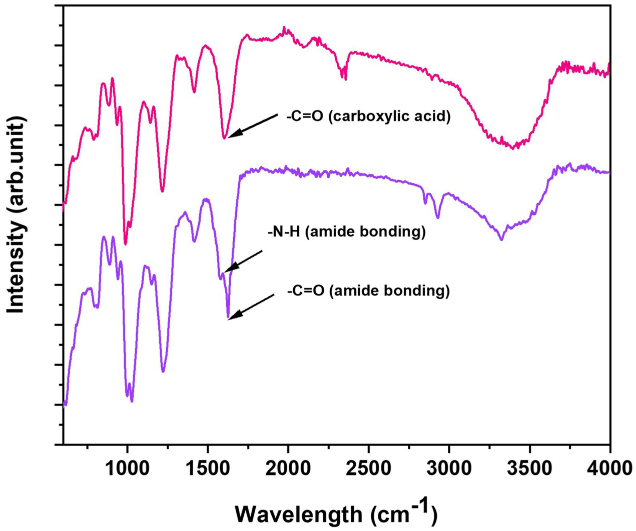

Figure 4 FTIR spectra comparing heparin (pink) with heparin-capped silver nanoparticles (purple). The analysis highlights the successful functionalization of heparin on the surface of silver nanoparticles.

nanoparticle core and heparin coating, though these are less intense in the spectrum of heparin alone. These results suggested that heparin was successfully conjugated to cyst-AgNPs via amide bond formation, which agreed with the results of the ^{1}H-NMR spectrum.

Surface Charge and Hydrodynamic Diameter by Dynamic Light Scattering (DLS)

The surface charge of nanoparticles, typically expressed as the zeta potential, plays a crucial role in determining their colloidal stability, cellular interaction, and biological performance. In the case of hep-AgNPs, the zeta potential is governed by the abundant sulfate ($–SO_3^-$) and carboxylate ($–COO^-$) groups present in the heparin polymer. These negatively charged functional groups impart a strong negative surface potential to the nanoparticle surface, thereby promoting electrostatic repulsion and reducing the likelihood of aggregation. Moreover, the surface charge can vary with the pH as the ionisation state of the acidic groups of heparin changes. Understanding the zeta potential behaviour of hep-AgNPs is essential for predicting their dispersion stability, interaction with biological membranes, and overall biocompatibility in various physiological environments. Therefore, the zeta potential of the hep-AgNPs was determined across a pH range of 2–9, as shown in Figure 5 (right). The results revealed that hep-AgNPs consistently maintained negative surface charges owing to the polyanionic nature of heparin. A clear trend was observed wherein zeta potential values became more negative with increasing pH, reaching a maximum of –33.1 mV at pH 8. This shift corresponds to enhanced ionisation of the carboxyl and sulfate functional groups of heparin under alkaline conditions. Notably, at physiologically relevant pH values (7–8), the zeta potential values exceeded − 30 mV, indicating excellent electrostatic repulsion and high colloidal stability. These results confirm the successful surface functionalization of hep-AgNPs and suggest that the nanoparticles remained well dispersed under near-physiological conditions, minimising the risk of aggregation during in vitro or in vivo use.

The hydrodynamic diameter of the hep-AgNPs was assessed by DLS across a pH range of 2–10 to evaluate their colloidal behaviour under different conditions (Figure 5, left). At acidic pH values (2–4), the nanoparticles exhibited significantly larger sizes (ranging from ~122 to 143 nm) and high polydispersity, indicating poor dispersion and aggregation. This was attributed to the protonation of the carboxyl and sulfate groups of heparin, which weakened the electrostatic repulsion necessary for a stable nanoparticle dispersion, in accordance with DLVO theory. As the pH increased toward neutrality (pH 5–7), a progressive decrease in size was observed, with the smallest and most monodisperse particles detected at pH 7 (~78.8 nm). This reflects the optimal ionisation of the heparin surface, which enhances the repulsive forces and improves colloidal stability. At alkaline pH levels (8–10), a gradual increase in size was observed (up to ~158 nm at pH 10), likely due to the conformational expansion of the heparin polymer or partial nanoparticle aggregation caused by high ionic content or charge shielding. These results demonstrate that hep-AgNPs are the most stable at neutral to mildly alkaline pH, supporting their suitability in physiological and biomedical environments.

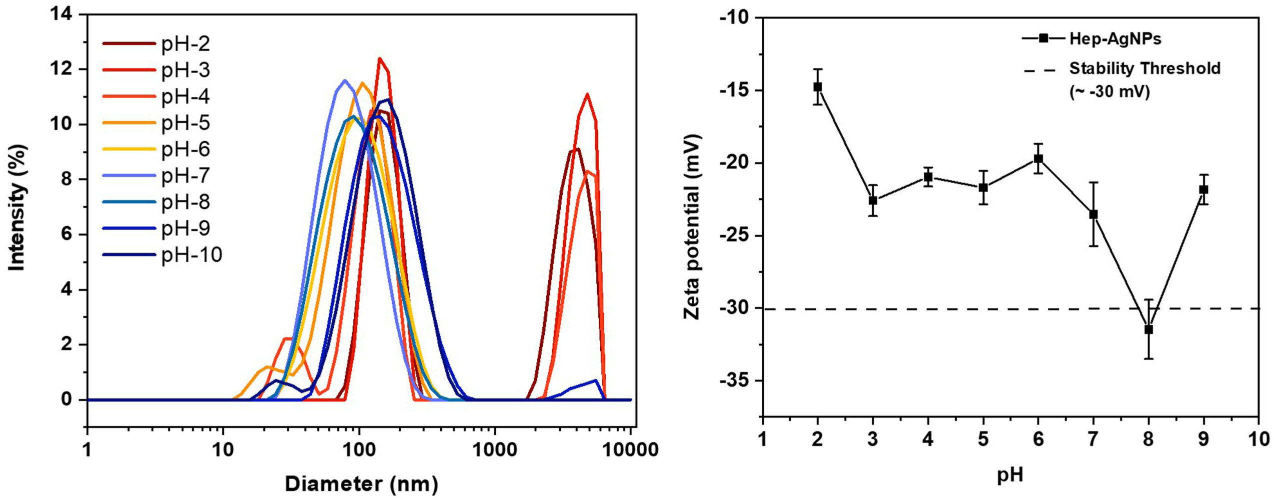

Figure 5 Left: DLS measurements showing the hydrodynamic size of hep-AgNPs across a pH range of 2–10, indicating size variation and aggregation behaviour under different pH conditions. Right: Zeta potential values of hep-AgNPs measured from pH 2 to 9, highlighting the influence of pH on surface charge.

Stability of Hep-AgNPs Across pH 2–9 Monitored by UV–Vis Spectroscopy

The long-term colloidal stability of the hep-AgNPs was assessed under varying pH conditions (2–9) for 11 days using UV–Vis spectroscopy, as shown in Figure 6. The absorbance at 450 nm, corresponding to the surface plasmon resonance (SPR) of the AgNPs, was used to monitor the dispersion and aggregation behaviour (Figure 6a–c). At acidic pH values (2–5), the absorbance decreases significantly over time, indicating progressive nanoparticle aggregation and potential sedimentation. The most pronounced instability was observed at pH 3 and 4, where the absorbance decreased to nearly zero after day 5. This trend is attributed to the protonation of heparin sulfate and carboxylate groups under acidic conditions, which reduces the electrostatic repulsion and facilitates aggregation.

In contrast, hep-AgNPs remained highly stable at near-neutral and alkaline pH values. At pH 7 and 8, the absorbance remained relatively constant, whereas at pH 9, a slight increase in absorbance was observed, suggesting an improved dispersion and potential polymer chain extension. These conditions favour full ionisation of the anionic groups of heparin, enhancing the nanoparticle surface charge and repulsion. This stability trend is consistent with the zeta potential measurements, which revealed the most negative surface charges (–25 to –33 mV) in the pH range of 7–9, correlating with minimal aggregation and optimal colloidal stability. Overall, these results demonstrated that hep-AgNPs exhibit the greatest long-term stability at physiological to mildly alkaline pH values, supporting their application in biological environments.

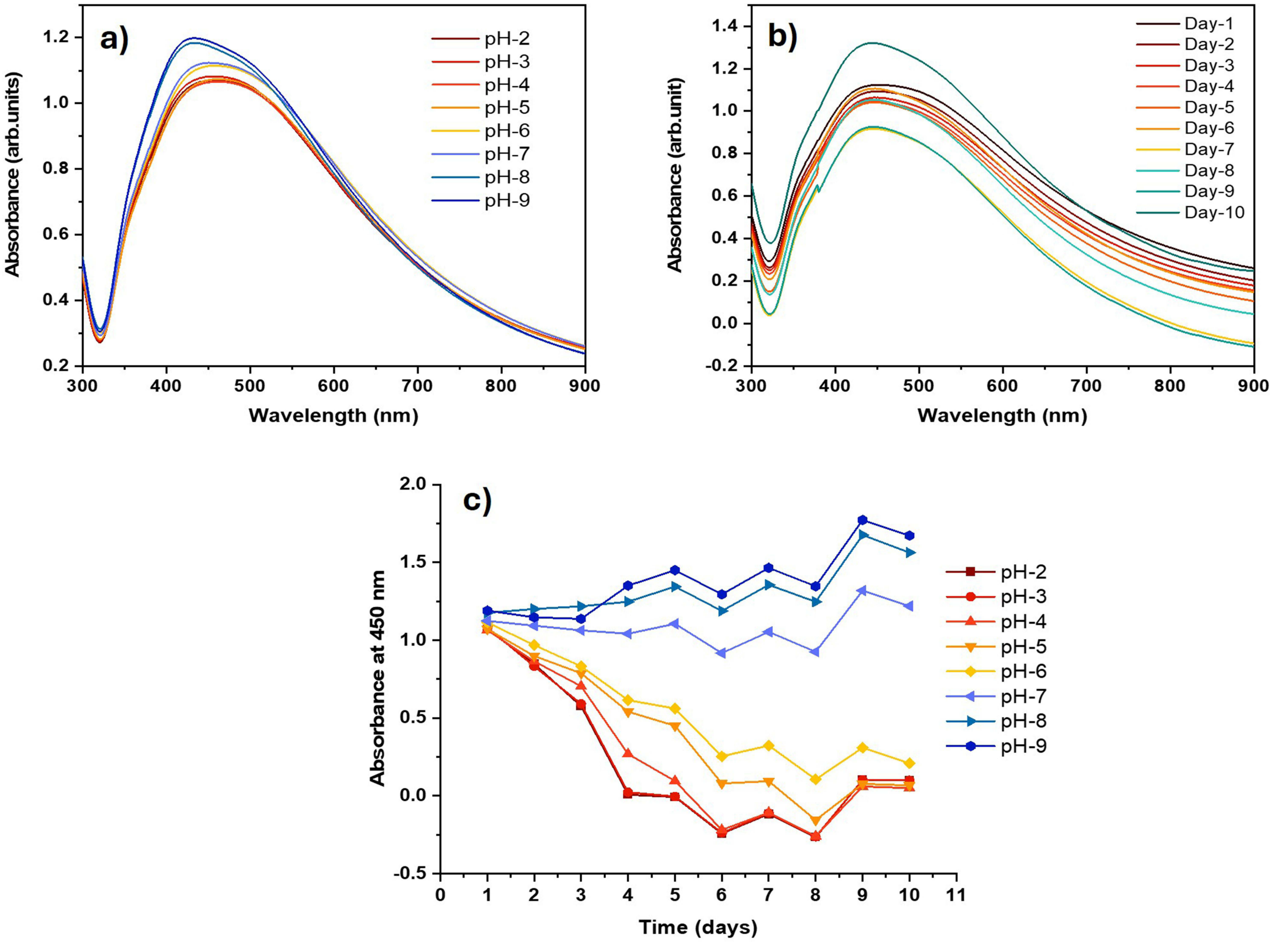

Figure 6 Stability of hep-AgNPs under varying pH conditions (2–9) evaluated by UV–Vis spectroscopy. (**a**) Absorbance spectra of hep-AgNPs at 450 nm across different pH environments, indicating pH-dependent colloidal stability. (**b**) Time-dependent UV–Vis spectra of hep-AgNPs at pH 7 over a 10-day period, demonstrating stable dispersion at physiological pH. (**c**) Absorbance at 450 nm plotted over 10 days for each pH condition, highlighting decreased stability under acidic conditions and improved stability at neutral to alkaline pH.

Cytotoxicity in Cancer Cells

The cytotoxic potential of the hep-AgNPs was assessed in both cancerous and non-cancerous breast cell lines (Figure 7), including MCF-7 (breast cancer), MDA-MB-231 (triple-negative breast cancer), and MCF-10A (normal mammary epithelial cells). These results demonstrate a clear distinction between the response of cancerous and non-cancerous cells to hep-AgNP treatment.

Notably, hep-AgNPs exhibited no significant cytotoxicity toward MCF-10A cells, even at concentrations as high as 100 µg/mL, indicating a favourable cytocompatibility profile within the tested concentration range. In contrast, dose- and time-dependent inhibition of cell viability was observed in both the MCF-7 and MDA-MB-231 breast cancer cell lines. In MCF-7 cells, viability decreased progressively with increasing nanoparticle concentration and exposure duration, consistent with effective cellular internalization and concentration-dependant cytotoxic effect of hep-AgNPs. The IC_{50} values at 24 h were estimated to be 78.65 µg/mL for MCF-7 cells and 97.55 µg/mL for MDA-MB-231 cells, which further decreased to 41.23 µg/mL for MCF-7 cells and 102 µg/mL for MDA-MB-231 cells after 48 h of treatment. As the IC_{50} for MCF-10A cells was not reached (>100 µg/mL), the selectivity index was expressed as a lower bound. Accordingly, selectivity indices of >2.4 for MCF-7 cells and >1 for MDA-MB-231 cells at 48 h were obtained, indicating favourable, concentration-dependent selectivity toward cancer cells relative to normal breast epithelial cells.

These differential effects between cancerous and normal cells suggest preferential uptake or susceptibility of cancer cells to hep-AgNPs, potentially owing to higher metabolic activity, increased membrane fluidity, or enhanced nanoparticle internalization via endocytic pathways. The presence of heparin on the nanoparticle surfaces may also enhance selective targeting through electrostatic interactions with cancer cell surfaces, which are often more negatively charged. Overall, these results demonstrate the selective cytotoxicity of hep-AgNPs, with enhanced activity towards aggressive breast cancer phenotypes, compared to non-cancerous cells at lower concentrations, highlighting their potential for dose-controlled and targeted nanotherapeutic development.

Antibacterial Potential

Optical Density Measurement for the Antimicrobial Test

The antibacterial activity of the hep-AgNPs was further evaluated quantitatively by measuring the optical density (OD600) of *S. typhimurium* at a wavelength of 600 nm for gram-negative bacteria after 24 h incubation in LB broth (Figure 8), *S. typhimurium* was treated with increasing concentrations of hep-AgNPs (0–80 µg/mL). As shown in Figure 8, untreated bacterial cultures (control) reached an OD600max of approximately 1.0, indicating robust bacterial

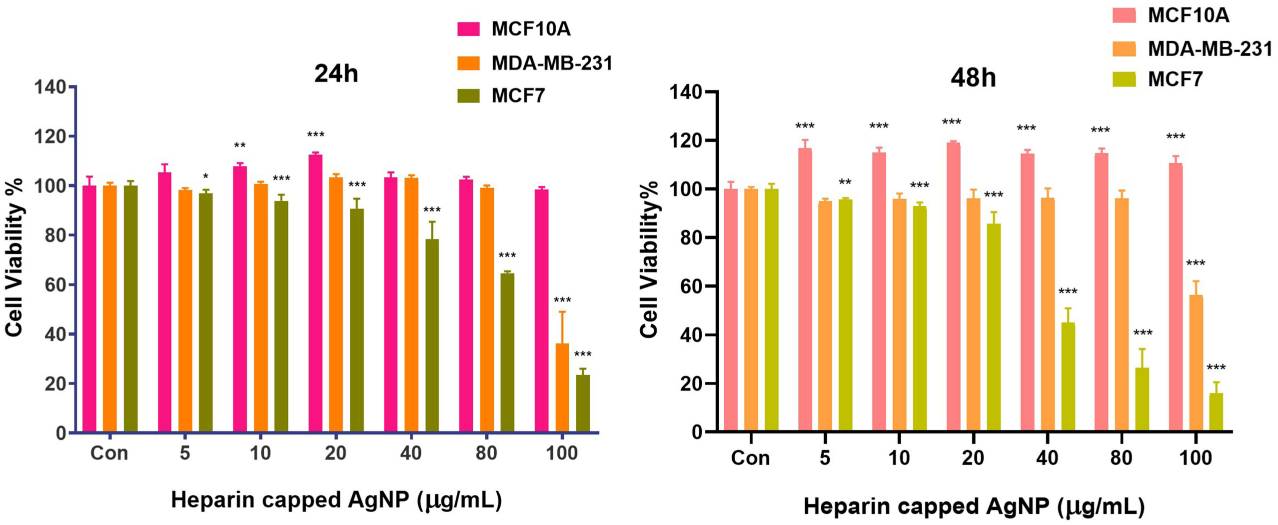

Figure 7 Displaying the in vitro cytotoxicity of hep-AgNPs assessed in normal and breast cancer cell lines. Data are presented as mean ± SD (n=6). Statistical significance was determined using a Two-way ANOVA with Dunnett's multiple comparisons test. $^*p < 0.05$, $^{**}p < 0.01$, and $^{***}p < 0.001$ indicate significant differences compared to the untreated control.

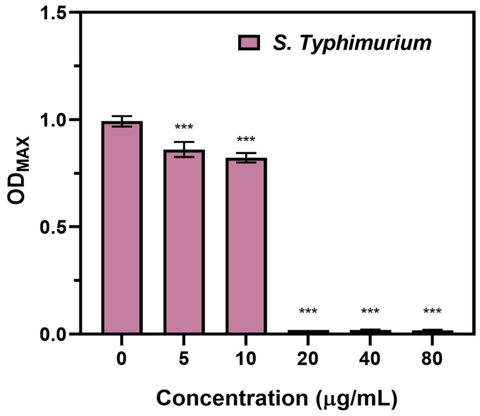

Figure 8 Optical density (OD_{600}) measurements showing the growth inhibition of *S. typhimurium* treated with varying concentrations of hep-AgNPs. Experiments were performed in triplicate, and error bars represent SD (±0.02). Statistical significance was determined using a One-way ANOVA with Dunnett's multiple comparisons test. ***$p < 0.001$ indicate significant differences compared to the untreated control.

growth. At low concentrations (5 and 10 µg/mL), moderate inhibition was observed, with OD 600max values reduced to 0.86 and 0.82, respectively. However, at 20 µg/mL and above, bacterial growth was almost completely suppressed, with the OD600max approaching zero. These results demonstrated a clear dose-dependent inhibition of *Salmonella* growth by hep-AgNPs, with a sharp decline in viability above 10 µg/mL, suggesting strong bactericidal activity. These data support the potential of hep-AgNPs as effective antimicrobial agents against gram-negative pathogens and indicate a minimum inhibitory concentration (MIC) of approximately 20 µg/mL.

To further evaluate the antibacterial activity of hep-AgNPs, growth inhibition assays were conducted on *E. coli* JM109 using a range of concentrations (1–320 µg/mL), shown in Supplementary Figure 2b, OD600max readings taken after 4 and 48 hours indicate a strong dose-dependent suppression of bacterial growth. At 4 h, hep-AgNPs significantly inhibited *E. coli* proliferation at concentrations ≥20 µg/mL, with complete suppression observed at concentrations ≥ 80 µg/mL. The calculated IC_{50} at 4 hours was 24.3 mg/L, indicating high potency at the early time points. Interestingly, the IC_{50} shifted to ~62 mg/L after 48 h, suggesting partial recovery or tolerance mechanisms after prolonged exposure, likely due to nanoparticle agglomeration or adaptive stress responses.

The OD max data from *E. coli* JM109 corroborate these findings, showing strong inhibition beyond 10 µg/mL, with near-complete growth suppression from 20 µg/mL onwards. Collectively, these data confirm the potent bactericidal action of hep-AgNPs against gram-negative strains. The early phase effectiveness (lower IC_{50} at 4 h) may be particularly valuable for acute antimicrobial interventions, whereas dose-dependent inhibition supports the potential of hep-AgNPs as broad-spectrum antibacterial agents. These findings are consistent with previous data obtained for *S. typhimurium*, reinforcing the antimicrobial efficacy of the formulation across multiple bacterial models.

Minimum Inhibitory Concentration (MIC) of Hep-AgNPs

The MIC values of Hep-AgNPs were determined using a broth microdilution assay against *S. typhimurium* 140285 and methicillin-susceptible *Staphylococcus aureus*. For *S. typhimurium*, the MIC of Hep-AgNPs was 16 µg/mL, indicating moderate antimicrobial activity. In comparison, the positive control ampicillin demonstrated a significantly lower MIC of 1 µg/mL, whereas the water control showed no inhibitory effect (>512 µg/mL), confirming the absence of antimicrobial activity from the solvent. For *S. aureus*, Hep-AgNPs exhibited a MIC of 8 µg/mL against S. aureus, demonstrating promising antibacterial efficacy. Ampicillin, the positive control, exhibited an MIC of <0.5 µg/mL, which was lower than that of Hep-AgNPs, suggesting a stronger antimicrobial effect of the antibiotic in this case. However, both bacterial strains were susceptible to Hep-AgNPs at concentrations suitable for potential therapeutic applications. These results underscore the effectiveness of Hep-AgNPs as a potential antimicrobial agent against both gram-negative and gram-positive bacteria, with the ability to inhibit bacterial growth at concentrations lower than that of the negative control

https://doi.org/10.2147/IJN.S576538

(water), yet not as potent as the antibiotic ampicillin. This suggests that Hep-AgNPs could serve as a promising adjunct or alternative for antimicrobial therapies, particularly against resistant strains.

Antifungal Assays

The antifungal efficacy of hep-AgNPs was evaluated against *C. albicans* and *A. fumigatus* at 24 and 48 h using a resazurin-based metabolic viability assay in accordance with EUCAST guidelines. The dose–response curves (Figure 9) demonstrate the concentration- and time-dependent inhibition of fungal viability by hep-AgNPs.

At 24 hours, *C. albicans* exhibited an MIC_{50} of 24.4 µg/mL and an MIC_{90} of 100 µg/mL, indicating a moderate antifungal effect within the early exposure period. For *A. fumigatus*, the MIC_{50} at 24 hours was 6.2 µg/mL, while the MIC_{90} was 50 µg/mL, suggesting relatively higher sensitivity to the nanoparticles at this stage.

After 48 h of treatment, antifungal activity slightly decreased. The MIC_{50} value for *C. albicans* increased to 86.8 µg/mL. However, it should be noted that the standardised endpoint for *C. albicans* susceptibility testing was 24 hours, not 48 hours. In contrast, *A. fumigatus* retained growth inhibition at 48 h, MIC_{50} of 16.45 mg/L a sharp decline in viability at concentrations ≥40 µg/mL, indicating a cumulative effect over prolonged exposure.

Collectively, these results highlight the potent and time-dependent antifungal activity of hep-AgNPs. Antifungal activity, particularly against *A. fumigatus*, may stem from prolonged nanoparticle–cell interactions, leading to membrane damage, oxidative stress, and disruption of fungal morphology. The combined properties of silver and heparin likely contribute to the observed antifungal activity through enhanced stability, cellular interactions, and uptake, positioning hep-AgNPs as promising candidates for addressing persistent fungal infections.

Phase-contrast microscopy analysis was performed to visually assess the antifungal effects of Hep-AgNPs against *C. albicans* and *A. fumigatus* after 24-hours and 48-hours treatment period (Figure 10). At sub-inhibitory concentrations, *C. albicans* displayed dense clusters of yeast cells with active budding and hyphal growth (12.5 µg/mL, top right panel), whereas *A. fumigatus* exhibited extensive mycelial networks with branching hyphae (12.5 µg/mL, bottom right panel). Upon treatment with increasing concentrations of Hep-AgNPs (from right to left), a progressive reduction in cell density and morphological integrity was observed in both the fungi. In *C. albicans*, Hep-AgNPs reduced budding in a dose-dependent manner, as evidenced by the sparse distribution of the cells.

At 100 µg/mL, yeast appeared unable to bud, as evidenced by the sparsely distributed cells. Similarly, in *A. fumigatus*, low doses resulted in reduced hyphal growth after 24 h, whereas 100 µg/mL Hep-AgNPs completely inhibited germination. After 48 h, the accumulation of Hep-AgNPs was apparent in germlings treated with 25–100 µg/mL due of their dark gray appearance. These morphological changes corroborate the metabolic inhibition data and confirm the

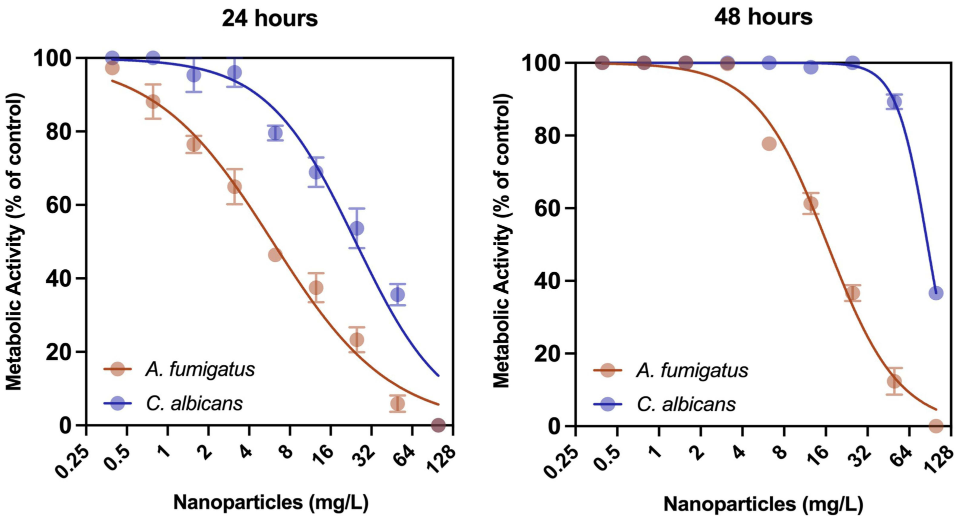

Figure 9 Dose–response curves showing the antifungal activity of hep-AgNPs against *C. albicans* (blue) and *A. fumigatus* (Orange) following 24 and 48 hours treatments. Fungal viability was assessed using a resazurin based metabolic assay according to EUCAST guidelines. The results demonstrate a concentration and time dependent reduction in fungal metabolic activity. Experiments were performed in triplicate; error bars represent standard errors.

https://doi.org/10.2147/IJN.S576538

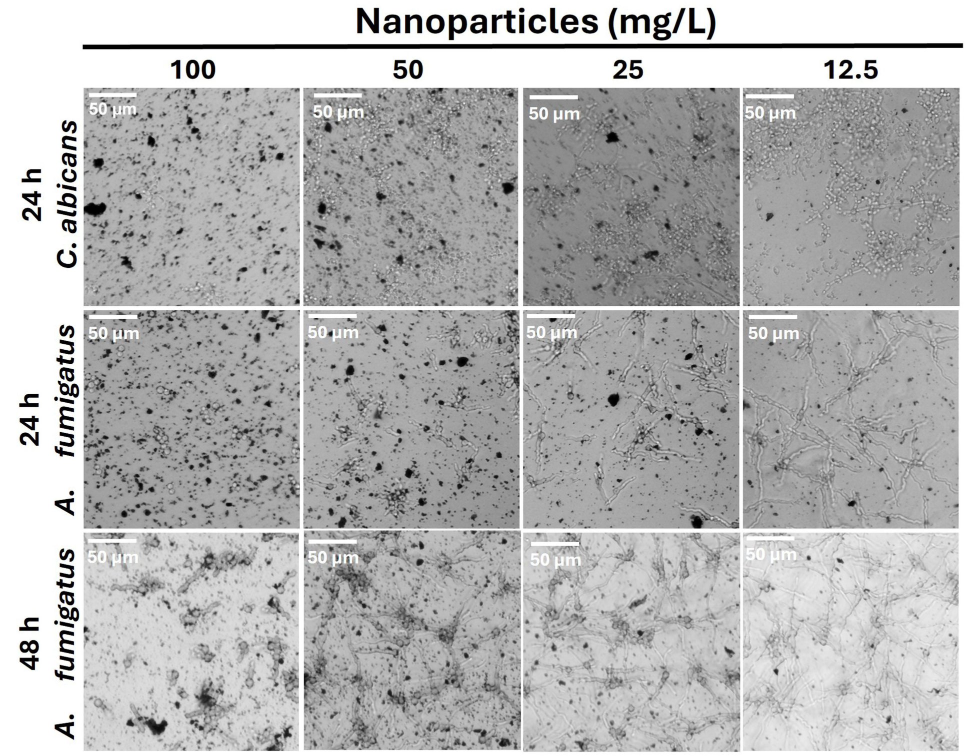

Figure 10 Representative phase contrast microscopy images showing the morphological effects of hep-AgNPs on *Candida albicans* and *Aspergillus fumigatus* after 24 and 48 hours of treatment at various concentrations. Images illustrate dose- and time-dependent inhibition of fungal growth and hyphal development. Scale bar = 50 µm.

potent antifungal activity of Hep-AgNPs. Overall, phase-contrast microscopy provides qualitative validation of the antifungal efficacy observed in quantitative MIC assays, supporting the role of Hep-AgNPs as a promising broad-spectrum agent. Overall, the data confirmed the broad-spectrum antifungal potential of Hep-AgNPs, highlighting their capacity to effectively inhibit both unicellular and filamentous fungal pathogens while offering a biocompatible alternative to conventional silver salts.

Uptake Assay by ICP-MS

Quantitative assessment of Hep-AgNP uptake was performed across different biological systems, including mammalian cancer cells (MDA-MB-231), fungal pathogens (*C. albicans* and *A. fumigatus*), and gram-negative bacteria (*S. typhimurium*). The internalised silver content was determined using ICP-MS and normalised to the nanograms of silver per cell (Figure 11).

The intracellular accumulation of Hep-AgNPs was quantified in mammalian, fungal, and bacterial cells using ICP-MS, revealing a time-dependent uptake profile across all the tested organisms (Figure 11).

Fungal uptake profiles revealed higher levels of internalization. In *C. albicans*, the silver uptake began at 8.62 ng/cell at 3 hours and increased to 8.87 ng/cell at 48 hours, peaking at 14.83 ng/cell at 24 hours before slightly decreasing at 48 hours. While *A. fumigatus* exhibited an initial uptake of 2.65 ng/cell at 3 hours and increased to 9.10 ng/cell at 48 hours (Figure 11a). The superior uptake by *A. fumigatus* is likely attributable to its more porous and dynamic cell wall structure. Heparin's highly anionic character and structural mimicry of natural glycosaminoglycans may enable robust interactions with fungal surface components such as mannoproteins, β-glucans, and chitin. These interactions are likely to promote nanoparticle adhesion and facilitate internalization via endocytosis-like or passive mechanisms. This significant intracellular accumulation suggests that hep-AgNPs are capable of effectively penetrating fungal cells, further supporting their potential use in antifungal therapy.

In MDA-MB-231 triple-negative breast cancer cells, Ag uptake increased steadily from 0.021 ng/cell at 0 h to 0.256 ng/cell at 24 h (Figure 11b), demonstrating efficient and progressive internalization. This enhanced uptake is likely driven by heparin surface modification, which facilitates cellular interactions through electrostatic binding to cell-surface proteins such as

https://doi.org/10.2147/IJN.S576538

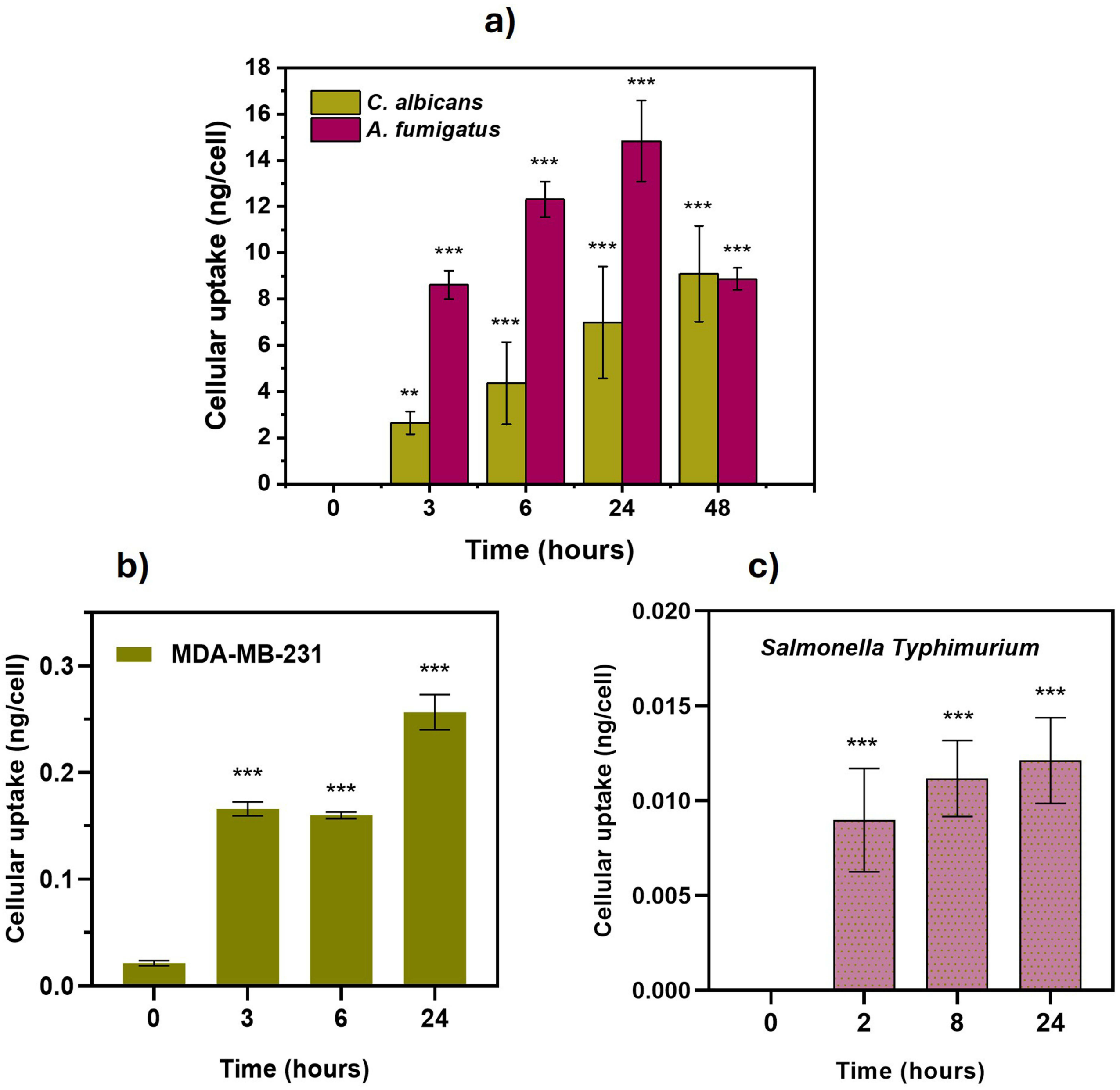

Figure 11 Intracellular uptake of hep-AgNPs measured by ICP-MS. (**a**) Fungal uptake in *C. albicans* and *A. fumigatus* over 3–48 hours; (**b**) Uptake by MDA-MB-231 breast cancer cells over 0–24 hours; (**c**) Uptake by *S. typhimurium* over 0–24 hours. Data are expressed as ng of silver per cell. Results demonstrate time-dependent accumulation across all organisms, with notably higher uptake in fungal and cancer cells. Experiments were conducted in triplicate; error bars represent standard deviation (±0.005–0.5). Statistical significance was determined using a Two-way ANOVA with Dunnett's multiple comparisons test (**a**), and One-way ANOVA with Dunnett's multiple comparisons test (**b** and **c**). $^{**}p < 0.01$, and $^{***}p < 0.001$ indicate significant differences compared to the zero hour.

syndecans, integrins, and heparan sulfate proteoglycans (HSPGs). Internalization is plausibly mediated via clathrin-dependent endocytosis and macropinocytosis—mechanisms that are upregulated in TNBC cells.[60] The efficient nanoparticle uptake observed here underscores the potential of heparin-functionalized systems as delivery platforms for targeted therapeutic applications.

In gram-negative *S. typhimurium*, a gradual time-dependent uptake was observed, beginning at 0.009 ng/cell at 2 h and reaching ~0.0121 ng/cell at 24 h (Figure 11c). Despite the inherent barrier posed by the outer membrane in gram-negative bacteria, these values are consistent with or exceed the previously reported silver nanoparticle uptake levels in bacterial cells, which typically range from femtograms to low picograms per cell.[61–63] The relatively higher uptake observed in this study may be attributed to heparin capping, which enhances nanoparticle affinity and membrane translocation through ionic interactions and potential membrane destabilisation. Importantly, these results demonstrated that hep-AgNPs are capable of associating with and penetrating bacterial cells, which is a key feature for effective antimicrobial activity.

Overall, the selective uptake profiles observed in cancer, fungal, and bacterial cells highlight the versatility of heparin as a nanoparticle capping agent. The substantial intracellular accumulation in cancer and fungal cells supports the therapeutic potential of hep-AgNPs in oncology and infectious disease applications, whereas the lower bacterial uptake at sub-inhibitory concentrations may be advantageous in minimising off-target cytotoxicity. Collectively, these observations support uptake-mediated mechanisms of AgNP activity, as outlined in the Introduction, and underscore the critical role of surface engineering particularly heparin functionalization in modulating bio–nano interactions and cellular internalization.

Discussion

Silver nanoparticles (AgNPs) have garnered considerable attention in biomedicine because of their broad-spectrum antimicrobial, anticancer, and antiviral properties. Their unique physicochemical characteristics, including a high surface-area-to-volume ratio and reactive oxygen species (ROS) generation capability, enable them to interact effectively with microbial membranes and cellular components, making them potent candidates for therapeutic interventions. However, challenges, such as colloidal instability, non-specific toxicity, and limited cellular selectivity, necessitate strategies to enhance biocompatibility and functional precision.

In this study, we synthesised and characterised heparin-capped AgNPs (hep-AgNPs) and evaluated their potential as multifunctional therapeutic platforms. The novelty of this study lies in the use of heparin—commonly known for its anticoagulant properties—as both a stabilising and functionalising agent for AgNPs, enabling enhanced biological interactions and improved functional performance. Heparin, a clinically approved biocompatible polysaccharide, is known for its anticoagulant properties. In addition to its classical role, heparin is emerging as a versatile biomolecule in nanomedicine because of its ability to interact with various growth factors, extracellular matrix proteins, and cell surface receptors, such as syndecans and heparan sulfate proteoglycans (HSPGs). Functionalization with heparin confers stability to AgNPs in biological environments and enables their specific interactions with mammalian and microbial cells.

The integration of heparin onto the surface of AgNPs represents a complementary functionalization strategy that combines the well-established antimicrobial properties of silver with the biological affinity and targeting capabilities of heparin towards cancer. This combination can enhance the functional performance of AgNPs by improving cellular interaction, uptake, and retention, while offering opportunities for dose-controlled and selective therapeutic applications. Heparin is known to interact with components of the tumour microenvironment, including pathways associated with angiogenesis and cell–matrix interactions, which may influence cellular responses in a context-dependent manner. Similarly, its affinity for microbial adhesion molecules and biofilm-associated matrices supports the observed enhancement in antifungal and antibacterial activity.

Despite these multifaceted benefits, the dual action potential of heparin-capped AgNPs remains underexplored. Few studies have investigated their therapeutic applicability to both cancer cells and pathogenic microbes. Our findings contribute to filling this gap by demonstrating not only the synthesis and stability of hep-AgNPs, but also their effective cellular internalization and biological activity across diverse systems, including triple-negative breast cancer cells (MDA-MB-231), fungal pathogens (*C. albicans* and *A. fumigatus*), and gram-negative bacteria (*S. typhimurium*).

Beyond their intrinsic selective cytotoxic and antimicrobial activity, hep-AgNPs may also be envisioned as versatile nanocarrier platforms for the delivery of additional therapeutic cargos. The efficient and progressive cellular uptake demonstrated across mammalian, fungal, and bacterial systems suggests that surface-functionalized AgNPs could be adapted for the transport of nucleic acid–based therapeutics, including microRNA, siRNA, or synthetic mRNA constructs, where intracellular delivery is a critical barrier. Recent advances such as microRNA-responsive split RNA switches for cell-type-specific regulation, programmable synthetic mRNA circuits, and DNA nanostructure-based delivery systems illustrate how nanoparticle-mediated uptake can be integrated with molecular-level control mechanisms to achieve enhanced selectivity and precision.[64–66] In this context, hep-AgNPs offer a complementary inorganic platform

https://doi.org/10.2147/IJN.S576538

that combines efficient internalization with modular surface chemistry, supporting future development of multifunctional and targeted nanotherapeutic delivery strategies.

Hep-AgNPs were successfully synthesised by amide coupling by reacting heparin with amine-terminated AgNPs (cyst-AgNPs). The synthesised hep-AgNPs were characterised using various techniques including FTIR, NMR, DLS, SEM, TGA, XRD diffraction. Initially, we hypothesised that heparin binds directly to nanoparticles, as illustrated in Scheme 1. However, after careful analysis of the reaction conditions, particularly the ratio of cyst-AgNPs to heparin, we observed that while an amide bond formed between heparin and cyst-AgNPs, heparin wrapped around the surface of the AgNPs. This observation made it challenging to determine the optimal ratio of heparin to cyst-AgNPs for the reaction. The goal was to fully coat the nanoparticle surface with heparin without using an excessive amount, which would be inefficient and wasteful.

Therefore, hep-AgNPs were synthesised using various ratios of heparin to cyst-AgNPs (1:1, 1:2, 1:4, and 1:12), and their effects on HaCaT and L929 cell lines, as well as on *E. coli* JM109 bacteria were investigated.

The Supplementary Figure 1 shows the cytotoxicity profiles of hep-AgNPs with varying Ag: heparin ratios in HaCaT and L929 cells over 24 and 48 h. The 1:1 ratio exhibited the highest cytotoxicity in L929 cells, with an IC_{50} of approximately 20 µg/mL, whereas HaCaT cells showed a comparatively better tolerance. Notably, 1:2 Ag:Hep ratio demonstrated reduced cytotoxicity and improved biocompatibility, suggesting that it is more suitable for applications that require lower toxicity to normal cells. The 1:4 ratio showed intermediate toxicity, whereas the 1:12 ratio exhibited minimal toxicity but reduced antimicrobial potency.

Further antibacterial screening against *E. coli* (Supplementary Figure 2a–d) confirmed that the 1:1 and 1:2 Ag:Hep ratios exhibited comparable IC_{50} values, while the 1:4 and 1:12 ratios were significantly less effective, indicating diminished bactericidal activity, likely due to excessive heparin coverage that sterically and electrostatically shields the silver surface and limits effective nanoparticle–cell interactions. Such overcoating may also hinder cellular uptake and attenuate Ag^+ release, thereby diminishing biological efficacy despite improved colloidal stability. These findings highlight the importance of optimising polymer coverage to balance surface protection with functional bioactivity, explaining why intermediate heparin loadings (eg 1:2 ratio) provided superior overall performance. Time-dependent assays using the 1:1 Ag:Hep formulation (Supplementary Figure 2b) revealed an increase in IC_{50} from 4 h to 48 h, suggesting partial bacterial recovery over prolonged exposure. This behaviour may reflect a predominantly bacteriostatic response at lower concentrations, bacterial adaptive stress responses, and/or time-dependent changes in nanoparticle dispersion in nutrient-rich media, underscoring the importance of exposure duration and dosing strategy. Comparative analysis with silver nitrate ($AgNO_3$, Supplementary Figure 2e) demonstrated an IC_{50} of 3.7 mg at 4 h, indicating that Ag^+ ions elicit only transient growth inhibition of *E. coli*. Collectively, these findings support the 1:2 Ag:Hep formulation as the optimal ratio, offering a balance between effective antibacterial activity and reduced cytotoxicity. These results underscore the dual utility of heparin: it not only serves as a capping and stabilising agent for AgNPs, but also enhances biological interactions through its reported anti-adhesive, anti-migratory, and anti-angiogenic activities, which are particularly relevant in cancer and infection-associated pathologies. The functionalization-mediated enhancement observed for heparin-capped AgNPs highlights their potential as a multifunctional nanoplatform.

Structurally, the size of the cyst-AgNPs varied between 4 and 10 nm, with most nanoparticles measuring approximately 10–11 nm. The molecular weight of heparin is 15 kDa, which corresponds to a hydrodynamic size of 2–3 nm in solution. Based on the surface area of the 10–11 nm nanoparticles (~314–380 nm^2), it is estimated that 2–3 heparin molecules are required to effectively wrap and functionalize the nanoparticle surface. These calculations also suggest that a 1:2 ratio of heparin to nanoparticles is theoretically sufficient for optimal surface coverage, although experimental conditions may influence the exact requirements.

The formation of hep-AgNPs was confirmed by UV–Vis spectroscopy, which showed a characteristic surface plasmon resonance (SPR) peak at approximately 400 nm, indicating well-dispersed and stable nanoparticles. FTIR and ^1H NMR analyses verified the successful covalent conjugation of heparin to cyst-capped AgNPs via amide bond formation, as evidenced by the distinct stretching bands corresponding to –CONH– linkages and chemical shift changes in the proton environment of heparin.

SEM revealed a uniform spherical morphology with a core diameter of 10–11 nm, whereas DLS measurements indicated a hydrodynamic diameter of approximately 90 nm, reflecting a hydration shell and surface-bound heparin. The zeta potential remained consistently negative (~ –30 mV) across the physiological pH range (7–9), confirming the colloidal stability due to electrostatic repulsion. Additionally, UV–vis monitoring for over 11 days showed no significant aggregation, supporting long-term stability under biologically relevant conditions.

The EDS spectra exhibited strong elemental silver peaks, verifying nanoparticle formation, whereas the XRD profiles showed sharp crystalline peaks for AgNPs, along with a characteristic broad hump around 24°, indicative of heparin coating. Importantly, no signals corresponding to silver oxide were observed, suggesting effective prevention of Ag core oxidation via heparin capping. TGA revealed distinct thermal degradation patterns between heparin and hep-AgNPs, further supporting successful surface modification.

Zeta potential measurements demonstrated that hep-AgNPs possessed a stable surface charge of –30 mV at pH 7, correlating with excellent colloidal stability. UV–Vis spectroscopy over 11 days across pH 2–9 confirmed that the nanoparticles retained dispersity under physiological to mildly alkaline conditions, which are characteristic of many chronic wound microenvironments. In contrast, aggregation was observed under acidic conditions ($pH < 5$).

Notably, acid-triggered aggregation following cellular internalization—such as within lysosomal compartments—may influence intracellular silver ion release and contribute to uptake-mediated cytotoxic mechanisms. However, the implications of such pH-responsive behaviour require further investigation to distinguish beneficial intracellular effects from delivery-related limitations, minimal aggregation was observed in the pH range of 7–9, which is most relevant to extracellular biological environments.

A limitation of this study is the potential presence of trace low–molecular weight species, such as residual MES buffer or EDC/NHS-derived byproducts, following centrifugal purification, which may influence surface-sensitive measurements. Nevertheless, the key conclusions—successful heparin conjugation, colloidal stability at physiological pH, and concentration-dependent biological responses—are supported by multiple complementary characterisation techniques and consistent biological trends. Future studies will incorporate extended dialysis-based purification to further minimise residual impurities.

In vitro cytocompatibility and cytotoxicity assessments revealed that hep-AgNPs exhibited minimal toxicity toward normal breast epithelial MCF-10A cells, even at concentrations of up to 100 µg/mL. In contrast, a dose- and time-dependent reduction in cell viability was observed in the MCF-7 and MDA-MB-231 breast cancer lines, highlighting differential, concentration-dependent cytotoxic responses compared to non-cancerous cells. Particularly in TNBC cells (MDA-MB-231), ICP-MS analysis demonstrated time-dependent silver uptake, increasing from 0.021 ng/cell (0 h) to 0.256 ng/cell (24 h), suggesting the effective intracellular delivery of hep-AgNPs. This selective uptake is likely mediated by electrostatic interactions between heparin sulfate/carboxyl groups and overexpressed cell surface proteoglycans (eg syndecans and HSPGs), followed by internalization via clathrin-mediated endocytosis and macropinocytosis, which are upregulated in TNBC.

ICP-MS data further revealed pronounced intracellular silver accumulation in fungal pathogens. In *A. fumigatus*, silver uptake increased from 2.65 ng/cell (3 h) to 9.10 ng/cell (48 h), whereas *C. albicans* exhibited even greater accumulation, 8.62 ng/cell at 3 hour peaking at 14.83 ng/cell (24 h) before slightly declining at 48 hours. Despite this difference in absolute accumulation, *A. fumigatus* displayed markedly greater sensitivity (lower IC_{50}), suggesting a strong structure–function relationship between fungal cell wall architecture, nanoparticle internalization, and biological response. Filamentous fungi such as *A. fumigatus* possess a more porous and dynamically remodeled cell wall compared to yeast cells, which may facilitate more effective intracellular access and silver-mediated toxicity per internalised dose.

Notably, the partial attenuation of antifungal efficacy observed at extended incubation times (48 h) may reflect either adaptive fungal responses to prolonged silver exposure or time-dependent changes in nanoparticle behaviour under biological conditions, such as aggregation or surface modification. While sustained intracellular silver accumulation supports continued nanoparticle association, further studies will be required to distinguish between fungal adaptation and physicochemical effects influencing antifungal activity over time. The enhanced interaction of heparin with fungal cell wall components, including mannoproteins, β-glucans, and chitin, likely promotes nanoparticle association and uptake through hydrogen bonding and electrostatic attraction, contributing to the potent antifungal activity observed.

In *S. typhimurium*, time-dependent internalization of hep-AgNPs was also observed, with silver uptake rising from 3.9×10^{-5} ng/cell at 0 h to 0.0121 ng/cell at 24 h. Although absolute uptake values were lower than those in fungal or mammalian cells, this level is considered significant based on literature benchmarks. Prior studies have reported the bacterial uptake of AgNPs in the femtogram (fg) to low picogram (pg) range per cell. The higher values observed here (~10 pg/cell) highlight the potential of heparin as an effective vector for bacterial membrane association and penetration. The polyanionic nature of heparin may disrupt the bacterial outer membrane or facilitate electrostatic attraction to positively charged surface components, thereby enhancing nanoparticle entry.

Together, these findings underscore the importance of nanoparticle surface functionalization for modulating bio-nano interactions. Heparin not only confers colloidal stability and favourable cytocompatibility profiles but also enhances the intracellular uptake of AgNPs across a spectrum of biological systems, from bacteria to fungi to human cancer cells. By simultaneously evaluating selective cytotoxic responses and antimicrobial activity, this study addresses an underexplored area in the literature, where nanomaterials are typically developed for either oncological or infectious applications in isolation, despite the increased susceptibility of immunocompromised cancer patients to opportunistic infections. This versatility positions hep-AgNPs as a promising multifunctional nanoplatform for targeted antimicrobial applications and selective, dose-controlled cytotoxic strategies, particularly against hard-to-treat pathogens and treatment-resistant malignancies.

Despite these promising findings, several limitations should be acknowledged. Protein corona formation under serum-containing biological media was not explicitly assessed in this study and may influence nanoparticle surface presentation, uptake behaviour, and biological responses in complex physiological environments. In addition, in vivo stability, biodistribution, and clearance were not evaluated and may further impact translational performance. While the consistent uptake trends and selective biological responses observed here support the robustness of the current data, future studies will focus on characterising protein corona effects and in vivo behaviour to more fully define the therapeutic potential of hep-AgNPs.

Conclusion

In conclusion, this study presents the successful synthesis, functionalization, and detailed characterization of hep-AgNPs, and demonstrates their multifunctional therapeutic potential. Heparin, beyond its conventional role as an anticoagulant, possesses a diverse range of biological properties,[43] including anti-inflammatory, anticancer, and antimicrobial[21]—making it a valuable candidate for biomedical applications. When conjugated to AgNPs, heparin significantly enhances colloidal stability, biocompatibility, and cellular uptake in various biological models.

Importantly, systematic optimisation of the Ag:Hep ratio identified a 1:2 formulation as the most effective balance between antimicrobial potency and reduced cytotoxicity, highlighting the critical role of surface coverage in modulating biological performance.

The optimised hep-AgNPs exhibited selective cytotoxicity against MDA-MB-231 triple-negative breast cancer cells, while sparing normal epithelial cells. They also demonstrated potent antifungal efficacy against *C. albicans* and *A. fumigatus*, and effective antibacterial action against *S. typhimurium* by quantifying intracellular accumulation, as confirmed by ICP-MS.

Together, these findings position hep-AgNPs as a promising multifunctional nanoplatform for selective, dose-controlled cytotoxic strategies and targeted antimicrobial applications, while mechanistic insights into uptake behaviour and pH-responsive stability provide important considerations for future translational development. Future studies will focus on in vivo evaluation, receptor-mediated uptake mechanisms, long-term stability, and the potential integration of therapeutic payloads to further advance applications in cancer and infectious disease contexts.

From a translational perspective, hep-AgNPs could be readily integrated into clinically relevant dosage forms, including injectable or topical hydrogels, antimicrobial wound dressings, and surface coatings for medical devices. Such formulations may enable localised, dose-controlled delivery while minimising systemic exposure, which is particularly relevant for chronic wound management and infection-prone cancer settings. These formulation strategies will be explored alongside in vivo evaluation in future studies.

Data Sharing Statement

All data generated or analysed during this study are available from the corresponding author upon reasonable request.

Acknowledgments

The authors would like to sincerely thank the Daphne Jackson Trust, the Royal Society of Chemistry (RSC), and the University of East Anglia (UEA) for their support through the Daphne Jackson Fellowship scheme. Special thanks go to Isabelle Chambrier for her continuous support, valuable guidance, and constructive discussions throughout this work. The author also thanks Dr. Linda Troeberg (UEA) for generously supplying the L929 cells and Dr. Chris Morris (UCL) for providing the HaCaT cells.

Funding

This research was conducted under the Daphne Jackson Fellowship scheme, sponsored by the Royal Society of Chemistry and the University of East Anglia. The work was also supported by the Academy of Medical Sciences (SBF008\1046) and Biotechnology and Biological Sciences Research Council (BB/Y005058/1). In addition, part of this study was supported by a grant from Cancer Prevention Research Trust UK.

Disclosure

The authors report no conflicts of interest in this work.

References

1. Zhang L, Gu F, Chan J, Wang A, Langer R, Farokhzad O. Nanoparticles in medicine: therapeutic applications and developments. *Clin Pharmacol Ther*. 2008;83(5):761–769. doi:10.1038/sj.clpt.6100400
2. Haleem A, Javaid M, Singh RP, Rab S, Suman R. Applications of nanotechnology in medical field: a brief review. *Glob Health J*. 2023;7(2):70–77. doi:10.1016/j.glohj.2023.02.008
3. Patil SP, Burungale VV. 2 - Physical and chemical properties of nanomaterials. In: Thorat ND, Bauer J, editors. *Nanomedicines for Breast Cancer Theranostics*. Elsevier; 2020:17–31.
4. Ahire JH, Behray M, Webster CA, et al. Synthesis of carbohydrate capped silicon nanoparticles and their reduced cytotoxicity, in vivo toxicity, and cellular uptake. *Adv Healthcare Mater*. 2015;4(12):1877–1886. doi:10.1002/adhm.201500298
5. Ahire JH, Chambrier I, Mueller A, Bao Y, Chao Y. Synthesis of d-Mannose capped silicon nanoparticles and their interactions with MCF-7 human breast cancerous cells. *ACS Appl Mater Interfaces*. 2013;5(15):7384–7391. doi:10.1021/am4017126
6. Ahire JH, Wang Q, Coxon PR, et al. Highly luminescent and nontoxic amine-capped nanoparticles from porous silicon: synthesis and their use in biomedical imaging. *ACS Appl Mater Interfaces*. 2012;4(6):3285–3292. doi:10.1021/am300642m
7. Ahire JH, Wang Q, Tao Y, Chao Y, Bao Y. Amine-terminated silver nanoparticles exhibit potential for selective targeting of triple-negative breast cancer. *Appl Nano*. 2024;5(4):227–244. doi:10.3390/applnano5040015
8. Mody VV, Siwale R, Singh A, Mody HR. Introduction to metallic nanoparticles. *J Pharm Bioallied Sci*. 2010;2(4):282–289. doi:10.4103/0975-7406.72127
9. Coxon PR, Ahire JH, Ashby SP, Frogley MD, Chao Y. Amine-terminated nanoparticle films: pattern deposition by a simple nanostencilling technique and stability studies under X-ray irradiation. *Phys Chem Chem Phys*. 2014;16(12):5817–5823. doi:10.1039/C3CP55344B
10. Schröfel A, Kratošová G, Šafařík I, Šafaříková M, Raška I, Shor LM. Applications of biosynthesized metallic nanoparticles – a review. *Acta Biomater*. 2014;10(10):4023–4042. doi:10.1016/j.actbio.2014.05.022
11. Klębowski B, Depciuch J, Parlińska-Wojtan M, Baran J. Applications of noble metal-based nanoparticles in medicine. *Int J Mol Sci*. 2018;19(12):4031. doi:10.3390/ijms19124031
12. Khursheed R, Dua K, Vishwas S, et al. Biomedical applications of metallic nanoparticles in cancer: current status and future perspectives. *Biomed Pharmacother*. 2022;150:112951. doi:10.1016/j.biopha.2022.112951
13. Shahalaei M, Azad AK, Sulaiman W, et al. A review of metallic nanoparticles: present issues and prospects focused on the preparation methods, characterization techniques, and their theranostic applications. *Front Chem*. 2024;12:1398979. doi:10.3389/fchem.2024.1398979
14. Chandrakala V, Aruna V, Angajala G. Review on metal nanoparticles as nanocarriers: current challenges and perspectives in drug delivery systems. *Emergent Mater*. 2022;5(6):1593–1615. doi:10.1007/s42247-021-00335-x
15. Abou El-Nour KMM, Eftaiha A, Al-Warthan A, Ammar RAA. Synthesis and applications of silver nanoparticles. *Arabian J Chem*. 2010;3(3):135–140. doi:10.1016/j.arabjc.2010.04.008
16. Zhang XF, Liu ZG, Shen W, Gurunathan S. Silver nanoparticles: synthesis, characterization, properties, applications, and therapeutic approaches. *Int J Mol Sci*. 2016;17(9):1534. doi:10.3390/ijms17091534
17. Meher A, Tandi A, Moharana S, et al. Silver nanoparticle for biomedical applications: a review. *Hybrid Adv*. 2024;6:100184. doi:10.1016/j.hybadv.2024.100184
18. Bruna T, Maldonado-Bravo F, Jara P, Caro N. Silver nanoparticles and their antibacterial applications. *Int J Mol Sci*. 2021;22(13):7202. doi:10.3390/ijms22137202
19. Krishnan PD, Banas D, Durai RD, et al. Silver nanomaterials for wound dressing applications. *Pharmaceutics*. 2020;12(9):821. doi:10.3390/pharmaceutics12090821

20. Yuan Y, Ding L, Chen Y, Chen G, Zhao T, Yu Y. Nano-silver functionalized polysaccharides as a platform for wound dressings: a review. *Int J Biol Macromol*. 2022;194:644–653. doi:10.1016/j.ijbiomac.2021.11.108
21. Ahire JH, Wang Q, Rowley G, et al. Polyurethane infused with heparin capped silver nanoparticles dressing for wound healing application: synthesis, characterization and antimicrobial studies. *Int J Biol Macromol*. 2024;282(Pt 1):136557. doi:10.1016/j.ijbiomac.2024.136557
22. Heilman S, Silva LGA. Silver and Titanium nanoparticles used as coating on polyurethane catheters. *J Nano Res*. 2017;47:17–23. doi:10.4028/www.scientific.net/JNanoR.47.17
23. Thomas R, Mathew S, Nayana AR, Mathews J, Radhakrishnan EK. Microbially and phytofabricated AgNPs with different mode of bactericidal action were identified to have comparable potential for surface fabrication of central venous catheters to combat *Staphylococcus aureus* biofilm. *J Photochem Photobiol B*. 2017;171:96–103. doi:10.1016/j.jphotobiol.2017.04.036
24. Cheng L, Zhang K, Weir MD, Melo MA, Zhou X, Xu HH. Nanotechnology strategies for antibacterial and remineralizing composites and adhesives to tackle dental caries. *Nanomedicine*. 2015;10(4):627–641. doi:10.2217/nnm.14.191
25. Lee D, Lee SJ, Moon J-H, et al. Preparation of antibacterial chitosan membranes containing silver nanoparticles for dental barrier membrane applications. *J Ind Eng Chem*. 2018;66:196–202. doi:10.1016/j.jiec.2018.05.030
26. Correia TR, Figueira DR, de Sá KD, et al. 3D Printed scaffolds with bactericidal activity aimed for bone tissue regeneration. *Int J Biol Macromol*. 2016;93(Pt B):1432–1445. doi:10.1016/j.ijbiomac.2016.06.004
27. Castiglioni S, Cazzaniga A, Locatelli L, Maier JAM. Silver nanoparticles in orthopedic applications: new insights on their effects on osteogenic cells. *Nanomaterials*. 2017;7(6):124. doi:10.3390/nano7060124
28. Carbone M, Donia DT, Sabbatella G, Antiochia R. Silver nanoparticles in polymeric matrices for fresh food packaging. *J King Saud Univ Sci*. 2016;28(4):273–279. doi:10.1016/j.jksus.2016.05.004
29. Rao MMV, Mohammad N, Banerjee S, Khanna PK. Synthesis and food packaging application of silver nano-particles: a review. *Hybrid Adv*. 2024;6:100230. doi:10.1016/j.hybadv.2024.100230
30. Abazari M, Badeleh SM, Khaleghi F, Saeedi M, Haghi F. Fabrication of silver nanoparticles-deposited fabrics as a potential candidate for the development of reusable facemasks and evaluation of their performance. *Sci Rep*. 2023;13(1):1593. doi:10.1038/s41598-023-28858-9
31. Shah MA, Pirzada BM, Price G, Shibiru AL, Qurashi A. Applications of nanotechnology in smart textile industry: a critical review. *J Adv Res*. 2022;38:55–75. doi:10.1016/j.jare.2022.01.008
32. Ong WTJ, Nyam KL. Evaluation of silver nanoparticles in cosmeceutical and potential biosafety complications. *Saudi J Biol Sci*. 2022;29(4):2085–2094. doi:10.1016/j.sjbs.2022.01.035
33. Mussin J, Giusiano G. Biogenic silver nanoparticles as antifungal agents. *Front Chem*. 2022;10:1023542. doi:10.3389/fchem.2022.1023542
34. Ong WTJ, Nyam KL. Chapter 5 - Silver nanoparticles for cancer diagnosis and treatment of cancer. In: Kesharwani P, editor. *Silver Nanoparticles for Drug Delivery.* Academic Press; 2024:109–127.
35. Gomes HIO, Martins CSM, Prior JAV. Silver Nanoparticles as Carriers of Anticancer Drugs for Efficient Target Treatment of Cancer Cells. *Nanomaterials*. 2021;11(4):964. doi:10.3390/nano11040964
36. Liu Y, Li F, Guo Z, et al. Silver nanoparticle-embedded hydrogel as a photothermal platform for combating bacterial infections. *Chem Eng J*. 2020;382:122990. doi:10.1016/j.cej.2019.122990
37. Zhu H, Gablech E, Gablech I, Neuzil P. The collective photothermal effect of silver nanoparticles probed by a microbolometer. *Communicat Mater*. 2024;5(1):66. doi:10.1038/s43246-024-00509-0
38. Takáč P, Michalková R, Čižmáriková M, Bedlovičová Z, Balážová Ľ, Takáčová G. The role of silver nanoparticles in the diagnosis and treatment of cancer: are there any perspectives for the future? *Life*. 2023;13(2):466. doi:10.3390/life13020466
39. Swanner J, Fahrenholtz CD, Tenvooren I, et al. Silver nanoparticles selectively treat triple-negative breast cancer cells without affecting non-malignant breast epithelial cells in vitro and in vivo. *FASEB Bioadv*. 2019;1(10):639–660. doi:10.1096/fba.2019-00021
40. Ferdous Z, Nemmar A. Health impact of silver nanoparticles: a review of the biodistribution and toxicity following various routes of exposure. *Int J Mol Sci*. 2020;21(7):2375. doi:10.3390/ijms21072375
41. Noti C, Seeberger PH. Chemical approaches to define the structure-activity relationship of heparin-like glycosaminoglycans. *Chem Biol*. 2005;12(7):731–756. doi:10.1016/j.chembiol.2005.05.013
42. Barrowcliffe TW. *Heparin- a Century of Progress. 1st Ed. Handbook of Experimental Pharmacology.* Berlin, Heidelberg: Springer; 2012:XIV, 462.
43. Wang P, Chi L, Zhang Z, Zhao H, Zhang F, Linhardt RJ. Heparin: an old drug for new clinical applications. *Carbohydr Polym*. 2022;295:119818. doi:10.1016/j.carbpol.2022.119818
44. Jack H, Sonia SA, Jonathan LH, Valentin F. Guide to anticoagulant therapy: heparin. *Circulation*. 2001;103(24):2994–3018. doi:10.1161/01.cir.103.24.2994
45. Young E. The anti-inflammatory effects of heparin and related compounds. *Thromb Res*. 2008;122(6):743–752. doi:10.1016/j.thromres.2006.10.026
46. Ma SN, Mao ZX, Wu Y, et al. The anti-cancer properties of heparin and its derivatives: a review and prospect. *Cell Adh Migr*. 2020;14(1):118–128. doi:10.1080/19336918.2020.1767489
47. Atallah J, Khachfe HH, Berro J, Assi HI. The use of heparin and heparin-like molecules in cancer treatment: a review. *Cancer Treat Res Commun*. 2020;24:100192. doi:10.1016/j.ctarc.2020.100192
48. Rak J, Weitz JI. Heparin and angiogenesis: size matters! *Arterioscler Throm Vasc Biol*. 2003;23(11):1954–1955. doi:10.1161/01.ATV.0000100563.16983.19
49. Karam MB, El Khoury J, Chakar C, et al. Heparan-mimetics: potential agents of tissue regeneration for bone and periodontal therapies. *Med Novel Technol Devices*. 2021;11:100066. doi:10.1016/j.medntd.2021.100066
50. Galvan L. Effects of heparin on wound healing. *J Wound Ostomy Continence Nurs*. 1996;23(4):224–226. doi:10.1016/s1071-5754(96)90095-9
51. Olczyk P, Mencner Ł, Komosinska-Vassev K. Diverse roles of heparan sulfate and heparin in wound repair. *BioMed Res Int*. 2015;2015:549417. doi:10.1155/2015/549417
52. Shute JK, Puxeddu E, Calzetta L. Therapeutic use of heparin and derivatives beyond anticoagulation in patients with bronchial asthma or COPD. *Curr Opin Pharmacol*. 2018;40:39–45. doi:10.1016/j.coph.2018.01.006
53. Hogwood J, Gray E, Mulloy B. Heparin, heparan sulphate and sepsis: potential new options for treatment. *Pharmaceuticals*. 2023;16(2):271. doi:10.3390/ph16020271

54. Yang G, Yang L, Zhou X. Inhibition of bacterial swimming by heparin binding of flagellin FliC from Escherichia coli strain Nissle 1917. *Arch Microbiol*. 2023;205(8):286. doi:10.1007/s00203-023-03622-9
55. Cont D, Harm S, Schildböck C, et al. The neutralizing effect of heparin on blood-derived antimicrobial compounds: impact on antibacterial activity and inflammatory response. *Front Immunol*. 2024;15:1373255. doi:10.3389/fimmu.2024.1373255
56. Nurunnabi M, Khatun Z, Moon WC, Lee G, Lee YK. Heparin based nanoparticles for cancer targeting and noninvasive imaging. *Quant Imaging Med Surg*. 2012;2(3):219–226. doi:10.3978/j.issn.2223-4292.2012.09.01
57. Wu J, Zhu J, Wu Q, et al. Mussel-inspired surface immobilization of heparin on magnetic nanoparticles for enhanced wound repair via sustained release of a growth factor and M2 macrophage polarization. *ACS Appl Mater Interfaces*. 2021;13(2):2230–2244. doi:10.1021/acsami.0c18388
58. Kemp MM, Kumar A, Clement D, Ajayan P, Mousa S, Linhardt RJ. Hyaluronan- and heparin-reduced silver nanoparticles with antimicrobial properties. *Nanomedicine*. 2009;4(4):421–429. doi:10.2217/nnm.09.24
59. Oliva JM, Ríos de la Rosa JM, Sayagués MJ, Sánchez-Alcázar JA, Merkling PJ, Zaderenko AP. Solvent-assisted in situ synthesis of cysteamine-capped silver nanoparticles. *Adv Nat Sci*. 2018;9(1):015001. doi:10.1088/2043-6254/aa9de9
60. Yue-Xuan L, Hong-Bo P. Macropinocytosis as a cell entry route for peptide-functionalized and bystander nanoparticles. *J Control Release*. 2021;329:1222–1230. doi:10.1016/j.jconrel.2020.10.049
61. Guo Y, Baumgart S, Stärk HJ, Harms H, Müller S. Mass cytometry for detection of silver at the bacterial single cell level. *Front Microbiol*. 2017;8:1326. doi:10.3389/fmicb.2017.01326
62. Quevedo AC, Ellis LJA, Lynch I, Valsami-Jones E. Mechanisms of silver nanoparticle uptake by embryonic zebrafish cells. *Nanomaterials*. 2021;11 (10):2699.
63. Gimenez-Ingalaturre AC, Abad-álvaro I, Goñi P, Billimoria K, Goenaga-Infante H, Laborda F. Performance of single-cell ICP-MS for quantitative biodistribution studies of silver interactions with bacteria. *J Anal At Spectrom*. 2024;39(3):743–753. doi:10.1039/D3JA00378G
64. Liang Z, Hu Y, Li CY, Yau WL, Tan K, Kuang Y. VPg-based bidirectional synthetic mRNA circuits enable orthogonal protein regulation for high-resolution cell separation. *Chem Commun*. 2024;60(41):5427–5430. doi:10.1039/d4cc01725k
65. Jiang S, Ge Z, Mou S, Yan H, Fan C. Designer DNA nanostructures for therapeutics. *Chem*. 2021;7(5):1156–1179. doi:10.1016/j.chempr.2020.10.025
66. Abe I, Ohno H, Mochizuki M, Hayashi K, Saito H. Split RNA switch orchestrates pre- and post-translational control to enable cell type-specific gene expression. *Nat Commun*. 2025;16(1):5362. doi:10.1038/s41467-025-60392-2